LAPPEENRANTA UNIVERSITY OF TECHNOLOGY
School of Engineering Science
Laboratory of Green Chemistry

Nikolai Ponomarev

SYNTHESIS OF NOVEL CELLULOSE BASED NANOCOMPOSITES BY GREEN METHODS AND THEIR POSSIBLE USE AS ADSORBENTS

Examiners: Prof. Mika Sillanpää

Instructor: D.Sc. (Tech) Eveliina Repo

ABSTRACT

Lappeenranta University of Technology
School of Engineering Science
Laboratory of Green Chemistry

Nikolai Ponomarev

Synthesis of novel cellulose based nanocomposites by green methods and their possible use as adsorbents

Master Thesis

2017

64 pages, 35 figures, 7 tables

Examiners: Prof. Mika Sillanpää
Instructor: D.Sc. (Tech) Eveliina Repo

The aim of this work was to develop of novel cost-efficient nanocomposites synthesized by "green" methods with sufficient adsorption performance for heavy metal cations (Ni^{2+}, Cd^{2+}, Pb^{2+}), phosphorous (phosphates), and sulfur (sulfates). Especially, the goal was to find the most suitable nanocomposite material and the most environmentally friendly and inexpensive method to produce this material in order to verify its possible use in real applications.

Synthesis of nanocomposites was performed using microcrystalline cellulose (MCC), in PEG/NaOH solvent by a thermal-assisted method using layered double hydroxides (LDH) with various composition; iron oxide (III); manganese oxide (IV) and magnesium hydroxide (MH) as reinforcement. All of the materials had a structure of nanocomposites confirmed by TEM. The cellulose based material reinforced by magnesium hydroxide was selected for more detailed studies due to its appealing properties. Effects of time, temperature, and cellulose amount on its structure were investigated. Results of XRD, FTIR and EDS mapping showed that the materials composed of cellulose and magnesium hydroxide. And cellulose presented as a polymer matrix in the nanocomposites. TEM and SEM analyses showed an even distribution of MH nanostructures with various morphology in the produced materials.

Each of the studied materials were tested as adsorbents with sufficient adsorption performance. Most of the materials demonstrated excellent uptake of nickel, cadmium, lead, phosphorous, and sulfur.

The novel synthesis method used in this study is feasible, cost-efficient and environmentally friendly. Moreover, the studied materials showed excellent potential for the removal of both anionic and cationic pollutants from the wastewater.

Keywords: cellulose, nanocomposite, magnesium hydroxide, $Mg(OH)_2$, LDH, PEG/NaOH, adsorption

Table of Contents

ABBREVIATIONS AND PARAMETERS

CCD – charge-coupled device

CL – cellulose

DP – degree of polymerization

DMA – dimethylacetamide

DMSO – dimethyl sulfoxide

DSC – differential scanning calorimetry

DTA – differential thermal analyses

DTG – differential thermogravimetry

EDS – energy-dispersive X-ray spectroscopy

FTIR – Fourier transform infrared spectroscopy

ICP-OES - inductively coupled plasma optical emission spectrometry

LDH – layered double hydroxides

MCC – microcrystalline cellulose

MH – magnesium hydroxide

n – degree of polymerization

NC – nanocomposite

PEG – polyethylene glycol

SEM – scanning electron microscopy

TA – thermal analyses

TEM – transmission electron microscopy

TG – thermogravimetry

XRD – X-ray powder diffraction

Parameters

a - constant for each spectral line;

c – speed of light;

d_i– interplanar distance;

E – quantum energy difference;

h - Plank constant;

n - is an integer (the order of reflection);

R - Rydberg constant;

V – acceleration voltage;

Z - the atomic number of the element;

α - angle of incidence;

θ - the angle of the beam of rays on the atomic plane;

λ - wavelength;

ν - frequency of oscillations;

v – wavenumber;

σ - screening constant.

ACKNOWLEDGMENTS

I highly appreciate D. Sc. Eveliina Repo and Professor Mika Sillanpää for providing possibility to perform Master Thesis in Laboratory of Green Chemistry.

The Regional Council of South-Savo is thanked for the financial support.

Mikkeli 21.03.2017

Nikolai Ponomarev

1. Introduction

During the recent years, polymer nanocomposites have obtained significant attraction due to their incredible properties, such as, thermal, electrical, mechanical (Shilin Liu, Zhang, Zhou, & Wu, 2008), and adsorption (Hokkanen et al., 2014), etc. Nanocomposites are materials with structures with at least one dimension that does not exceed 100 nm. The properties of nanoparticles are dependent on their shape, size and surface area/volume ratio (Buzea, Blandino, & Robbie, 2007), which can be improved by integration of these nanoparticles on polymer matrix (Jeon & Baek, 2010). Nanocomposites could be successfully applied in wastewater treatment, electronics, biotechnology, medicine, catalysis, optics etc. (Eichhorn et al., 2010). A various (nano)composites have been obtained based on different synthetic polymers such as polyurethane (Jang, Min, Jeong, Lyoo, & Lee, 2008), polystyrene (X. Fu & Qutubuddin, 2000), methacrylate (Okamoto, Morita, Kim, Kotaka, & Tateyama, 2000), polyimide (Yano, Usuki, & Okada, 1997) and so on. However, synthetic polymers cause significant problems for environment due to their long lifespan higher than a few hundreds of years. Moreover, fabrication of synthetic polymers releases harmful pollutants and consists of usage of environmentally unfriendly, nonrenewable materials. Mentioned drawbacks have initiated the application of biodegradable natural polymers. Obviously, renewable materials have some considerable advantages compare to synthetic polymers due to their non-toxicity, transparency, and satisfactory durability.

Natural polymers for nanocomposites can be for example chitosan (Jahed, Khaledabad, Almasi, & Hasanzadeh, 2017), starch (Siyuan Liu et al., 2016), lignin (Kołodyńska, Gęca, Pylypchuk, & Hubicki, 2016) and cellulose (Han & Yan, 2010; Lefatshe, Muiva, & Kebaabetswe, 2017; Ma, Deng, & Yao, 2014). Cellulose is widely used as natural polymer matrix for nanocomposites because of its structure, cost efficiency and suitability for various applications.

Cellulose is the most common plant polymer on the earth and is the main component of the plants. Structural formula of cellulose is shown on Figure 1. This polysaccharide consists of linear chain of linked D-glucose units. The amount of two repeated glucose units is called degree of polymerization (DP) and can be from hundreds up to thousands (Fig. 1). DP is cellulose source and type of preparation dependent. For example, length of wood cellulose molecule with DP of several hundred is shorter compared to cotton cellulose with DP of several thousands. Moreover, cellulose crystallinity depend on factors, such as fabrication and source

as well. For example, cellulose after mercerization or dissolution process has different crystalline structure or even becomes amorphous compare to raw cellulose. Mentioned factors related to cellulose are important for this research topic. Cellulose does not have significant adsorption performance by itself, which is the reason for the need of reinforcement. Different type of reinforcements are studied in this work.

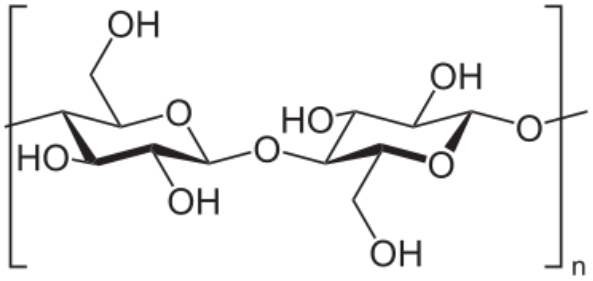

Figure 1. Structural formula of repeated cellulose unit, n – is degree of polymerization.

Recently, preparation of cellulose nanocomposites has engaged considerable attention. The materials produced and studied have been for example cellulose-hydroxyapatite (Grande, Torres, Gomez, & Carmen Bañó, 2009; Jia, Li, Ma, Sun, & Zhu, 2010), cellulose-layered double hydroxides (Iftekhar, Srivastava, & Sillanpää, 2017), cellulose-zinc oxide (Lefatshe et al., 2017), cellulose-titanium oxide (Marques, Trindade, & Neto, 2006), cellulose-Fe_2O_3 (Shilin Liu et al., 2008), cellulose-silica (Cai et al., 2012), cellulose-$CaCO_3$ (L. H. Fu et al., 2013), cellulose-gold (Zhang et al., 2010), cellulose-silver (Sureshkumar, Siswanto, & Lee, 2010), cellulose-manganese (Ma et al., 2014).

Many successful techniques including the sol-gel method (Siqueira, Mathew, & Oksman, 2011), solvothermal process (Nata, Sureshkumar, & Lee, 2011), freezing/freeze-drying method (Svagan, Jensen, Dvinskikh, Furó, & Berglund, 2010), UV-induced modification method (Attia et al., 2013), ultrasound method (L.-H. Fu, Yao, Shi, Ma, & Zhao, 2014), microwave-assisted method (Jia, Li, Zhu, et al., 2010) and hydrothermal method (Hokkanen et al., 2014) have been used for the synthesis of cellulose nanostructured materials.

Typically, dissolution of cellulose is required for the preparation of cellulose nanocomposites. Dissolving of cellulose can be performed by the several recent developed cellulose solvents, such as lithium chloride/*N*,*N*-dimethylacetamide (LiCl/DMAc) (Mccormick & Hutchinson, 1985), ammonium/ammonium thiocyanate (NH_3/NH_4SCN) (Cuculo, Smith, Sangwatanaroj, Stejskal, & Sankar, 1994), calcium thiocyanate ($Ca(SCN)_2$) (Hattori, Koga, Shimaya, & Saito, 1998), dimethyl sulfoxide (DMSO)/tertrabutylammonium floride (Heinze et al., 2000), LiOH/Urea and NaOH/Urea (Cai & Zhang, 2005) and PEG/NaOH (Yan & Gao, 2008), etc.

Some of cellulose solvent systems have been accepted to be applicable also for the cellulose (nano)composite preparation. The NaOH/Urea system was successfully applied for cellulose-hydroxyapatite (Jia, Li, Ma, et al., 2010), manganese-containing cellulose nanocomposite (Ma et al., 2014) and layered-double hydroxide intercalated cellulose nanocomposite (Iftekhar et al., 2017), etc. Also cellulose hydroxyapatite was synthesized in *N*,*N*-dimethylacetamide (DMAc) system (Ma et al., 2010). Cellulose–calcium silicate nanocomposites were prepared with success in LiCl/DMAc solvent (Li, Jia, Zhu, Ma, & Sun, 2010). PEG/NaOH solvent was used for preparation of all-cellulose composite film (Han & Yan, 2010).

One of the possible reinforcements for cellulose are layered double hydroxides (LDH) so-called anionic clays, which are hydrotalcite like layer-structured materials (Fig. 2). These hydroxides are compounds with structure of

$$[M^{2+}_{1-x}M^{3+}_{x}(OH)_2]^{x+}[A^{m-}_{\frac{x}{m}}\cdot nH_2O]^{x-} \quad (1)$$

where M^{2+}- cation of divalent metal, for example Mg^{2+}, Zn^{2+}, Mn^{2+} etc.; M^{3+}- cation of trivalent metal: Al^{3+}, Fe^{3+}, Cr^{3+} etc. and A^{m-} denotes - different anions such as, OH^-, CO_3^{2-}, NO_3^{2-}, ClO_4^- etc. Variables x and n can be widely varied. Structure of layered double hydroxides consists of positive charged hydroxide layers $[M^{2+}_{1-x}M^{3+}_{x}(OH)_2]^{x+}$ and interlayer $[A^{m-}_{\frac{x}{m}}\cdot nH_2O]^{x-}$. Interlayer consists labile anions and water molecules. The structure of LDH is also presented in Figure 2.

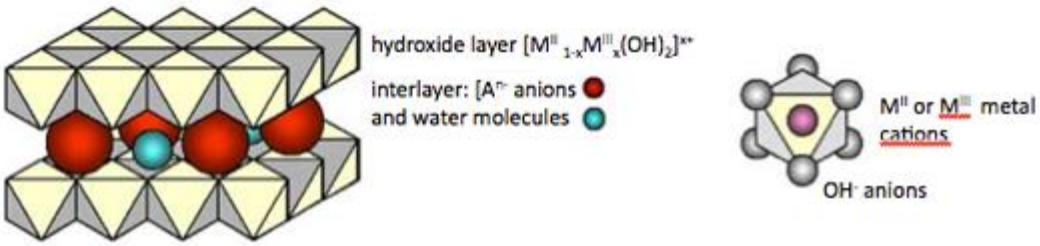

Figure 2. Structure of layered double hydroxides

LDH are widely used as adsorbents, catalysts, catalyst supports, medicine, flame retardant, ion exchanger etc. (Cavani, Trifiro, & Vaccari, 1991).

Other possible reinforcements for cellulose can be metal oxides or hydroxides. They are widely used as adsorbents (Hua et al., 2012), catalysts, flame retardants and so on. One of the most promising reinforcement is magnesium hydroxide. Brucite or magnesium hydroxide $Mg(OH)_2$ (MH) has a hexagonal symmetry (C6-type) with basic layered unit. Magnesium hydroxide has

various applications such as catalysis, fire retardants, water treatment, pharmacy, bleaching of cellulose, etc. (Wang et al., 2016; Zheng & Zhou, 2014). Also, $Mg(OH)_2$ is used as precursor for nano-sized magnesium oxide (Ding et al., 2001).

In this study, novel cellulose nanocomposites were obtained from microcrystalline cellulose by simple thermal-assisted method in green PEG/NaOH aqueous solution (Yan & Gao, 2008). The novel nanocomposites are cellulose-MH, cellulose-LDH, cellulose-$Fe(OH)_3$, manganese containing cellulose and cellulose-nano Fe_3O_4. Some of cellulose-LDH materials were produced by the co-precipitation method with further anion exchange method (Bish, 1980). Cellulose-$Fe(OH)_3$ nanocomposites were prepared by an unique redox method, a method, which is totally new approach in order to produce this kind of (nano)composites. PEG/NaOH cellulose solvent has the advantages such as cost-efficiency, less chemical consumption, and no formation of residual harmful side products compared to other cellulose solvents. Besides that, this solvent is not only applied for cellulose nanocomposites preparation but also influences on the fiber matrix. Moreover, polyethylene glycol in solvent system affects morphology and the particle size of intercalations (Zheng & Zhou, 2014). In this study, all of the mentioned materials were prepared and studied with FTIR and TEM in order to confirm the right composition and structure of nanocomposites. Also, all of the materials were preliminary tested as adsorbents with sufficient results. The most "green" material, cellulose-MH, was selected for further studies and optimization steps of its synthesis were performed. Optimized parameters were heating time, heating temperature, and cellulose concentration. The inexpensive starting materials and feasibility of the synthesis make mentioned methods promising for industrial applications.

Within recent years, nanocomposites have been widely studied in the water treatment applications (Hokkanen et al., 2014; Iftekhar et al., 2017). Especially, in these applications, materials should show high efficiency without causing any extra harm to the environment. Therefore, nanocomposites based on the natural polymers were tested in this study as adsorbents for the pollutant removal from the synthetic wastewater.

2. Analytical methods used for studies

2.1. Fourier transform infrared spectroscopy (FTIR)

Fourier transform infrared spectroscopy (FTIR) – is one of the methods of absorption spectroscopy. Having studied the position and intensity of the lines of the infrared spectrum of this substance, one can obtain information on the structure of its main structural groupings, the presence of certain functional groups in the structure of matter (Papko et al., 2013).

A molecule, like an atom, has a large number of different energy states which effects on the amount of energy absorbed by it. The transition of a molecule from one energy state into another is associated with the absorption or emission of light quanta with energy

$$E = hcv \quad (2)$$

h - Plank constant; E – quantum energy difference; c – speed of light; v – wavenumber.

When the frequencies of the vibrational motion of atoms in molecules coincide, the electromagnetic oscillations of the external radiation source resonance absorption of energy is observed, as a result of which the molecule passes from the lower (basic) vibrational level to one of the excited.

Atoms in solids fluctuate at a frequency of 1012-1013 Hz. Pairs or groups of interconnected atoms can be excited and are translated into higher energy states by absorbing radiation of the appropriate frequency. The absorption bands, associated with the excitation of vibrational energy levels, signals in the spectral range from 200-300 to 4000-5000 cm^{-1} (2-50 μm).

FTIR spectra are graphical dependence of the intensity of the absorbed IR radiation on the wave number, or wavelength. Typically, spectrums are written in coordinates: transmittance [%] – wavenumber [cm^{-1}]. The vibrations of bound atoms are divided into two main type: stretching and bending vibrations (Figure 3,4). The stretching vibrations are periodic displacements. (ν_s - symmetric and ν_{as} - asymmetric). Bending vibrations – are displacements

at straight angles to the bond (δ). If several normal vibrations occur identically but the displacements of the atoms are different, degeneration of vibrations is occurred.

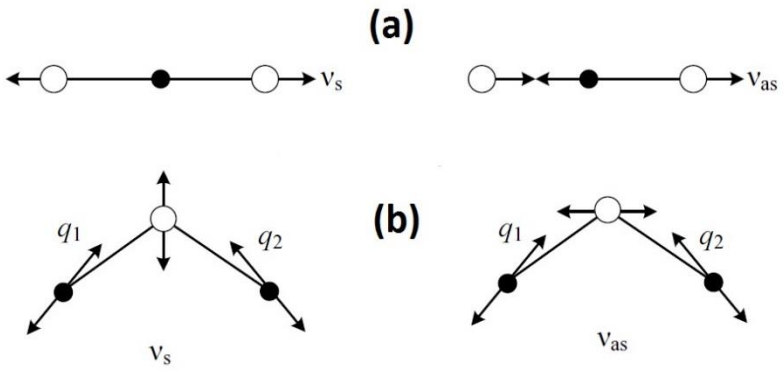

Figure 3. Stretching vibrations: (a) linear molecule; (b) nonlinear molecule.

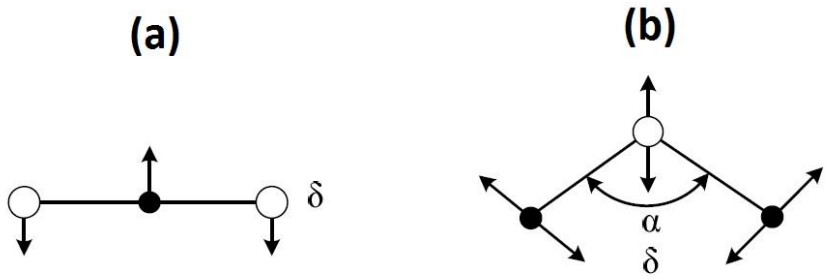

Figure 4. Bending vibrations: (a) linear molecule; (b) nonlinear molecule.

Interpretation of the obtained FTIR spectra is carried out by comparing them with the spectra of known substances. The possibilities of FTIR research are rather diverse. With the help of FTIR spectroscopy, the identification of substances is carried out, including the presence of impurities of crystalline substances that are not determined by the XRD because of the small concentration.

2.2.X-ray powder diffraction (XRD)

X-ray phase analysis (XRD) refers to diffraction methods of analysis. Diffraction methods are based on scattering of radiation or particle flux without changing their energy, i.e. on elastic scattering.

In the technology of inorganic materials, diffraction analysis methods are used mainly to determine the composition of crystalline phases present in natural and synthesized materials (ceramics, binders, raw materials and inorganic synthesis products).

With the help of X-ray phase analysis, the qualitative and quantitative compositions of materials are investigated, the parameters of the unit cell of crystalline substances are determined, and solid solutions and transformations that occur in materials during heat treatment are considered.

X-rays are one of the forms of electromagnetic radiation that occurs when a metal anode is bombarded with an electron beam. X-ray radiation is characterized by high penetrating power, since it has a short wavelength (0.1-0.5 nm).

Using X-ray studies of crystalline materials is based on the fact, that its wavelength is commensurate with the distance between atoms in a crystal lattice, that it is native for the diffraction grating. The rays scattered by different atoms interfere. The phenomenon of interference of scattered rays leads to the same result as the mirror reflection of the rays from the atomic planes of the crystal (Fig. 5). The amplification of the reflected X-ray intensity as a result of interference is observed if the path difference between parallel rays is equal to an integer number of waves.

The reflected rays propagate in a single phase (the intensity increases) if the Wulf-Bragg equation is satisfied:

$$n\lambda = 2d_i sin\theta \quad (3)$$

n - is an integer (the order of reflection); λ - wavelength of X-rays, nm; d_i – interplanar distance between two neighboring planes of a given family of parallel planes in a crystal), nm; θ - the angle of the beam of rays on the atomic plane.

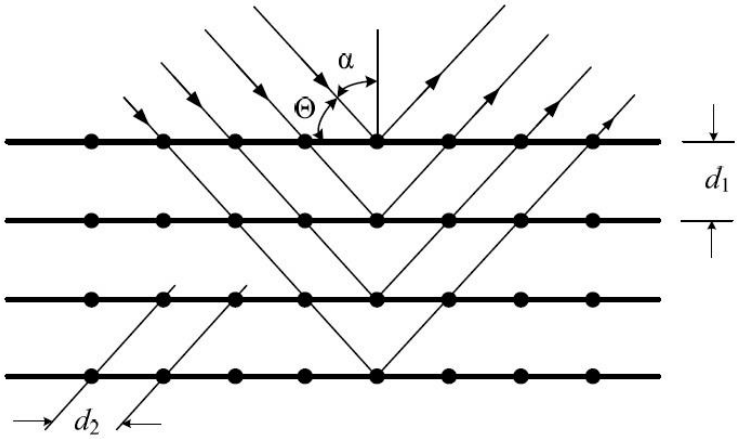

Figure 5. Reflection of X-rays from the atomic planes of the crystal: θ - angle of slip (Bragg angle); α - angle of incidence; d_1, d_2 - interplanar distances.

When the sliding angle changes, and the Wulf-Bragg equation is not observed, the reflected rays propagate in different phases and cancel each other.

X-ray diffraction pattern from a polycrystalline substance is the sum of diffraction patterns from individual crystals, randomly arranged relative to each other. Each crystal is characterized by a set of families of parallel atomic planes with interplanar distances d_1, d_2, ..., d_n.

For the appearance of a diffraction maximum, it is necessary that all parallel planes of a given family with an interplanar distance d_i are located at an angle θ with respect to the primary beam of X-rays.

Each crystalline substance is determined by its diffractogram or a set of values of interplanar distances and the intensity of the corresponding maxima. In a mixture of several substances, each of them produces its own X-ray diffraction pattern independently of the others. Therefore, the diffractogram of a mixture of crystalline substances is the sum of the diffractograms of all components.

The task of qualitative X-ray phase analysis is the determination (identification) of the type of crystalline phases contained in the material under study. The analysis is based on the fact that each crystalline compound gives a specific X-ray diffraction pattern with a specific set of diffraction maxima. Interplanar distances for most crystalline substances are established, and reference radiographs are given in the reference literature or database (Papko et al., 2013).

2.3.Electron microscopy

Electron microscopic investigation of inorganic substances and materials is used to study the features of their structure and phase composition.

The concept of structure describes a wide range of details. There are four scale levels of the structure - macrostructure, mesostructure, microstructure and nanostructure.
To the macro level there are features that are visible to the naked eye, the size of one millimeter to meters. Examples of macrostructural details are large pores, foreign inclusions and cracks that appear when the material shrinks.

The concept of mesostructure is introduced to describe features whose size is at the limit of the possibilities of the unaided eye (0.2-1 mm). To study this level, optical microscopy is used (the magnification is up to 10^3).

The concept of a microstructure encompasses details ranging in size from one to one hundred microns. This structural level includes micro and meso particles, the distance between the particles, microcracks and micropores. It is this level of structure that provokes the greatest interest of scientists and engineers. To study the microstructure, raster and transmission electron microscopy is used, as well as atomic force microscopy.

The term nanostructure refers to submicron-sized parts. It describes the width of grain boundaries, grains at the initial stage of crystallization, the region of existence of local order in amorphous bodies. The study of the nanoscale requires an increase in 10^9 and is carried out by transmission electron microscopy, X-ray diffraction, and scanning tunneling microscopy. The electron microscope uses an electron beam whose wavelength is 100 000 times shorter than the wavelengths of visible light. This provides the possibility of obtaining a much larger magnification than in the case of optical microscopy. The wavelength λ [nm], of the electron beam is determined from equation

$$\lambda = \frac{0.0388}{\sqrt{V}} \tag{4}$$

V – acceleration voltage, [V] (5 – 200 kV).

Modern high-resolution electron microscopes make it possible to obtain magnification up to 800 000 times, to observe the distribution of atoms in crystal lattices.

In transmission electron microscopy (TEM), the image is formed as a result of the passage of an electron beam through an electron-transparent sample.

As a result of the interaction of the primary electron beam with the sample surface, secondary electron emission can arise.

In this case, scanning electron microscopy (SEM) is used to obtain information about the objects under investigation, which makes it possible to obtain images of objects as a result of recording the secondary-electron flux.

The main difference between the principles of the transmission of a transmission electron microscope and a scanning electron microscope is related to the method of data collection and imaging. As in an optical microscope, in a transmission electron microscope, information from all points of the image is collected simultaneously, and the enlarged image is focused by means of lenses. In a scanning electron microscope, information is collected successively for each point as the primary electron beam moves (Papko et al., 2013).

2.3.1. Transmittance electron microscopy (TEM)

Transmittance electron microscopes are used to conduct studies using the TEM method. As can be seen from Fig. 6, the image is formed as a result of the passage of a beam of electrons through the analyzed sample. At the same time, fast electrons which are produced in modern models of microscopes an accelerating voltage of the order of 100-200 kV, are used.

The electron source is a heated tungsten filament, which creates an electron beam with a current density up to 5×10^4 A/m^2. Lanthanum hexaboride crystals (LaB_6) can also be used.

The electrons are emitted by an electron gun mounted at the top of the transmission electron microscope column. Inside the column, a high vacuum is maintained by evacuating the air. The electrons emitted by the gun are accelerated in the accelerator tube, passed through the lenses of the illuminator, and then fallen on the sample.

After passing through the sample of electrons in the objective lens system, an image is formed. Then the projection lens creates an enlarged image. As a result, the image formed on the fluorescent screen can be seen through the surveillance camera window. It can be recorded on a photographic film in a photographic camera or displayed on a computer monitor screen (Papko et al., 2013).

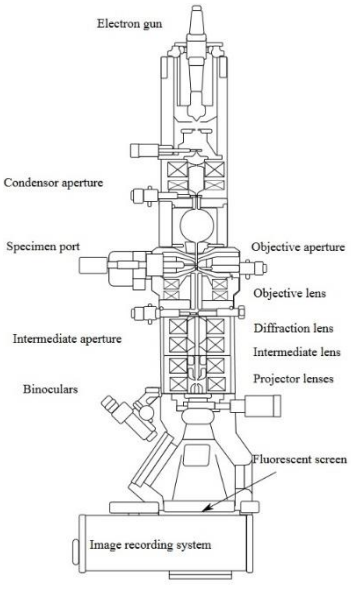

Figure 6. Schematic diagram of the transmission electron microscope.

2.3.2. Scanning electron microscopy (SEM)

The scanning electron microscope consists of an electron gun and a system of magnetic lenses. In SEM, a focused electron beam is deflected with a magnet and scanned over the surface of the sample, similar to a beam of electrons running a line after line on a television tube screen. In this case, secondary electrons are generated that arise as a result of the interaction of the scanning electron beam with the surface of a solid body.

The electron source is a thin tungsten filament heated by an electric current transmitted through it to a very high temperature. The electrons flowing from its tip pass through the cylinder of the electron gun, which receives a negative voltage (from 5 to 50 kV), and is compressed into a narrow beam. Due to the large potential difference between the cathode served by the cylinder of the electron gun and the anode, the electron beam receives a large acceleration. Fast-flying electrons fall into the magnetic field of the first condenser electromagnetic lens and are compressed into a dense stream that focuses on the sample area when using an objective electromagnetic lens. With this lens, you can change the diameter of the electronic probe.

The deflection system (scanning system) deploys the probe over a given area on the object. When the probe electrons interact with the object, several types of secondary interaction products arise, the signals from which can be registered by the corresponding detectors.

After conversion and amplification, these signals are visualized using a personal computer. The scan of the image in the monitor of the personal computer is made synchronously with the scanning of the electronic probe in the scanning electron microscope, and an enlarged image of the object is observed on the monitor screen.

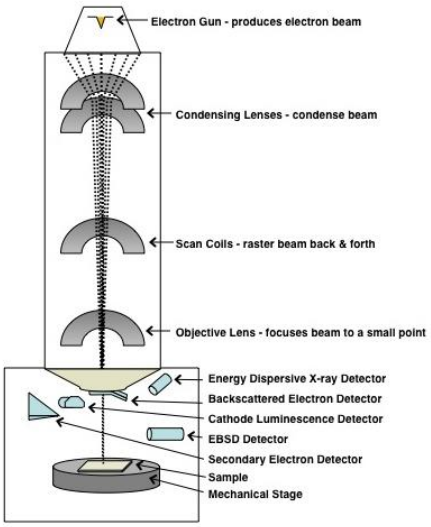

Figure 7. Scanning electron microscope scheme with EDS

The resolving power of the SEM is determined by: the cross-sectional area or the diameter of the probe, the contrast created by the sample and the detector system, the region of signal generation in the sample. Modern SEM achieve high perfection of design components, which allow to reduce the diameter of the probe to 5-10 nm.

Technical capabilities of SEM.

1. A scanning electron microscope allows one to directly study large areas of surfaces on massive samples in a wide range of magnifications - from 10 to 50 000 and higher with a sufficiently high resolution. In this case, it is not required, as for the TEM, to perform complex and lengthy replica manufacturing operations.

2. With SEM it is possible to investigate the general character of the structure of the entire surface. Object at small magnifications and to study in detail any region of interest to the researcher at large magnifications.

3. SEM has a large depth of focus, which allows you to observe a three-dimensional image of the structure with the possibility of its quantitative evaluation (Figure 8).

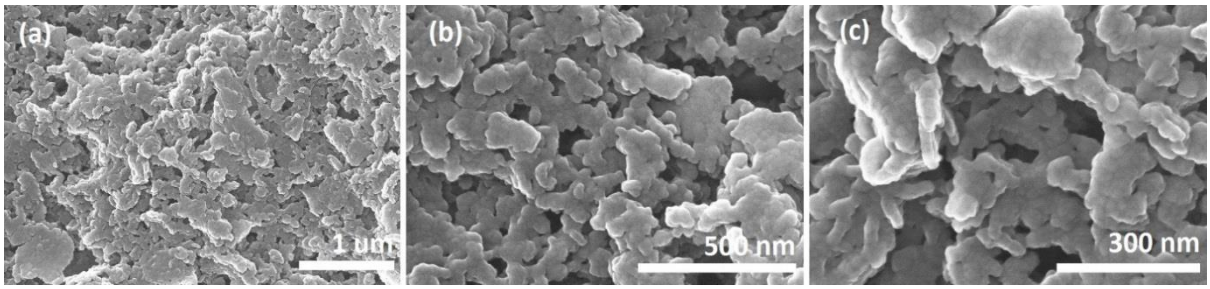

Figure 8. SEM image of cellulose based sample reinforced by magnesium hydroxide.

Conditions are created for direct study of the structure of surfaces with a highly developed relief, for example, kinks. SEM provides ample opportunities for studying the structure of materials, both monolithic and powders. The large depth of the SEM focus allows one to clearly and simultaneously observe powder particles that are very different in size, for example, with a particle radius of 0.05 μm and 1 mm.

4. At present, up to 60 consoles can be used for SEM various functional purposes. Usually SEMs are supplied with microanalysers of chemical composition, which makes it possible to conduct energy dispersive X-ray spectroscopy (EDS).

2.4. Energy-dispersive X-ray spectroscopy (EDS)

Energy-dispersive X-ray spectroscopy (EDS) allows local qualitative and quantitative elemental analyzes of the samples under study. As described above, one of the signals that result from the action of the electron beam on the sample is the characteristic X-ray radiation. The emission of X-rays occurs because of the bombardment of the sample surface by electrons. Thus for X-ray excitation spectrum using a beam of electrons with an energy of 10-30 keV and 1-2 microns in diameter (analysis of the "point") or a scanning electron beam - raster - of the size 10 × 10 and 500 × 500 mm (analysis surface area) .

The energy or wavelength of an X-ray quantum is characteristic of the element from which it was emitted. The energy of the X-ray photon is determined by the energy difference of the corresponding energy levels. K-radiation is the radiation that is formed when the K shell is filled; L-radiation is the radiation that is formed when the L-shell is filled, etc. (Fig. 9).

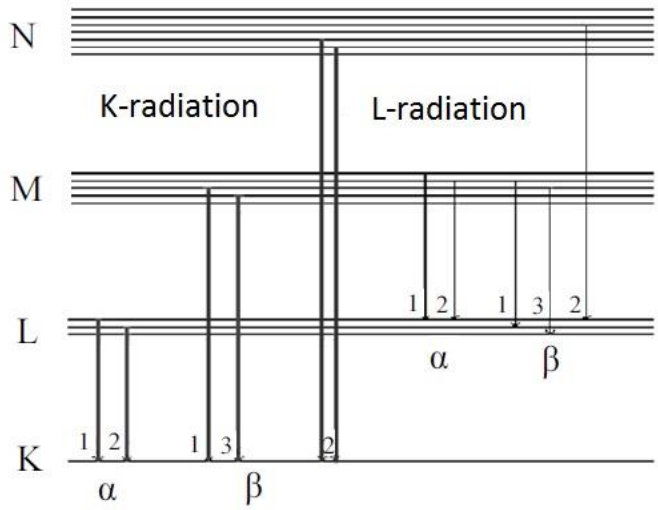

Figure 9. Determination of X-ray lines

The full designation of the emitted X-ray line also includes information about which shell the electron that fills the vacancy is. At the same time, Greek letters are used α,β,χ ... with the numbering 1, 2, 3, ... for the establishment of differences between different shells and sublevels. The most frequent transition of electrons from the L layer to the K layer is a 2p → 1s transition (K_α -radiation).

The difference in the energies of the electron levels of the atom is individual for any element, therefore, according to the position of the x-ray line in the spectrum, elements can be identified. The position of the line in the emission X-ray spectrum can be estimated on the basis of the Moseley law

$$\sqrt{\nu} = Ra(Z - \sigma) \quad (5)$$

ν - frequency of oscillations; Z - the atomic number of the element; R - Rydberg constant (3.29 $\cdot 10^{15}$ Hz); a - constant for each spectral line; σ - screening constant.

From the equation it follows that each type of atoms is characterized by a certain frequency of oscillations of the secondary X-rays excited by the primary radiation. To perform the analysis, it is necessary to determine the quantum energy or the wavelength of the characteristic X-ray radiation. Depending on the principle of operation, the system for analyzing characteristic X-ray radiation is distinguished by spectrometers with wave dispersion and spectrometers with energy dispersion.

Spectrometers with energy dispersion determine the energy of quanta of characteristic X-ray radiation and their number. For this purpose a cooled semiconductor detector - p-n-junction based crystal Si or Ge is used. The advantage of such spectrometers is a high analysis speed (several minutes), a disadvantage: a limited number of detectable elements, from Na to U. Spectrometers with wave dispersion use the phenomenon of X-ray diffraction incident on the crystal analyzer.

After excitation of the element in the sample, the set of wavelengths characteristic for the element leaves the sample. This secondary radiation falls on the crystal, which serves as a spectrum analyzer. The work of the crystal analyzer is based on the phenomenon of X-ray diffraction, described by the already discussed Wulf-Bragg law (formula 3). The scheme of X-ray diffraction on successive layers of atoms of the crystal analyzer surface is similar to that shown in Fig. 5. Depending on which element is to be determined and, accordingly, the wavelength of the analytical line, a crystal analyzer with a suitable distance between the atomic planes is selected. With the help of wave analysis, all elements, from beryllium (atomic number 4) to uranium, can be determined. X-ray radiation, reflected from the sample, falls into the counter. In spectrometers with wave dispersion, proportional or scintillation detectors are used. As a result, the X-ray spectrum is fixed.

Fig. 10 shows the spectrum of cellulose based magnesium reinforced sample obtained as a result of EDS using an electron microscope Hitachi S-4800 scanning electron microscope using 30 kV of acceleration voltage, with option of energy dispersive X-Ray spectrometer (EDS) operated at 30 kV. The background signal of the emission X-ray spectrum forms X-ray quanta that are inelastically scattered by electrons of solid-state atoms.

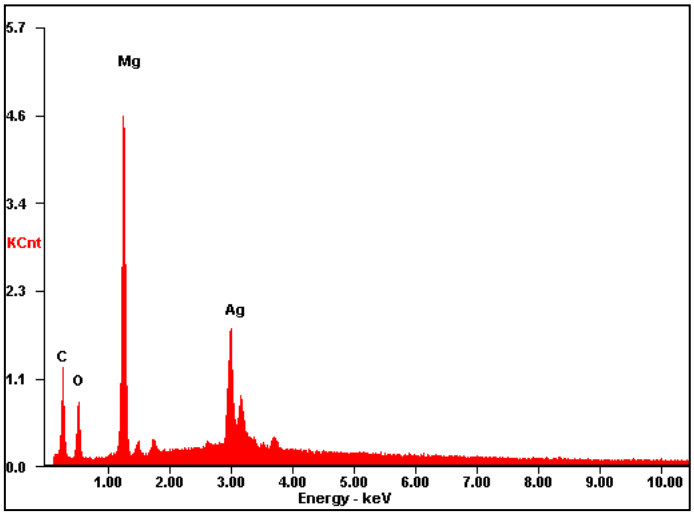

Figure. 10 EDS spectrum of cellulose based sample reinforced by brucite.

2.5.Thermal analyses

Thermal analysis is a method of studying physical-chemical and chemical processes based on recording the thermal effects that accompany transformations under conditions of temperature change.

In the high-temperature synthesis of nanocomposites, various physical and chemical processes occur, such as dehydration, decarbonization, melting, crystallization, polymorphic transformations, etc. These processes are accompanied by a change in the thermophysical properties of the materials. Therefore, the methods of thermal analysis are widely used in the study of phase transformations in the heating process, the construction of phase diagrams, and the study of the kinetics of chemical reactions. The results of thermal analysis are used to determine the optimal technological parameters for the synthesis of materials.

The main analysis methods are differential thermal (DTA), thermogravimetric (TG and DTG) and differential scanning calorimetry (DSC).

2.5.1. Differential thermal analysis (DTA)

Most physicochemical processes are accompanied by a change in the enthalpy of the system, i.e., thermal absorption effects (endothermic processes) or exothermic processes of heat release.

Endothermic effects are recorded when the following physicochemical processes occur: dehydration, decarbonization, decomposition of chemical compounds into simpler solid products, enantiotropic polymorphic transformations, and melting.

Exothermic effects correspond to the following physicochemical processes: oxidation, crystallization, the transition of matter from an unstable state to a stable, solid-phase reactions, monotropic polymorphic transformations, etc.

The principle of thermography is the fixation of thermal effects, manifested in an increase or decrease in the temperature of the system under study.

The simplest method of thermal analysis (TA) is to record the temperature change of a substance during its heating or cooling with a conventional thermocouple in the "temperature-time" coordinates. The release or absorption of heat in the test substance is manifested on the curves of simple recording in the form of areas or bends of the curves. The disadvantage of this method is its low sensitivity, which makes it impossible to obtain an accurate characterization of the studied processes, especially if they are accompanied by small thermal effects.

A more accurate and sensitive method is the differential recording of the heating or cooling curves used in DTA. In the DTA method, the temperature difference Δt is measured between the test substance and the reference sample, the standard in the heating or cooling mode. As a reference, a thermoactive substance - α-Al_2O_3 or MgO - is used. In these substances, when heated in the temperature range 20-1400 ° C, there are no transformations associated with changes in thermophysical properties.

Registration of the heat content of the substance is carried out using a differential thermocouple. The differential thermocouple consists of two thermocouples connected by the same ends of the wire and connected to the device, which fixes the change in the electromotive force circuit, which is formed when the thermocouple junctions are heated. One junction of such a combined thermocouple is placed in the substance under study (study sample), and the other in the standard. Fig. 11 shows the differential thermocouple circuit.

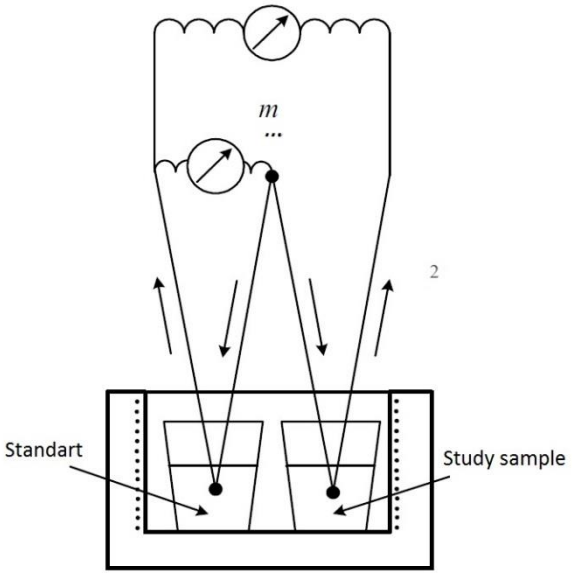

Figure 11. Scheme of differential thermocouple

At the same temperature of hot junctions, an electromotive force appears in the thermocouples, which is mutually compensated in the differential thermocouple. If hot junctions have different temperatures, then an uncompensated thermocouple arises in the circuit. At the beginning of the process, the temperature in the substance being analyzed increases or decreases in comparison with the reference temperature. As a result, maxima directed upwards or downwards will appear on the curve of the differential record.

The graphical dependence (curve DTA) is shown in Fig. 12. If, under heating, the substance under study does not experience any transformations associated with absorption or release of heat, the temperature difference will be zero. In this case, the DTA curve is registered as a

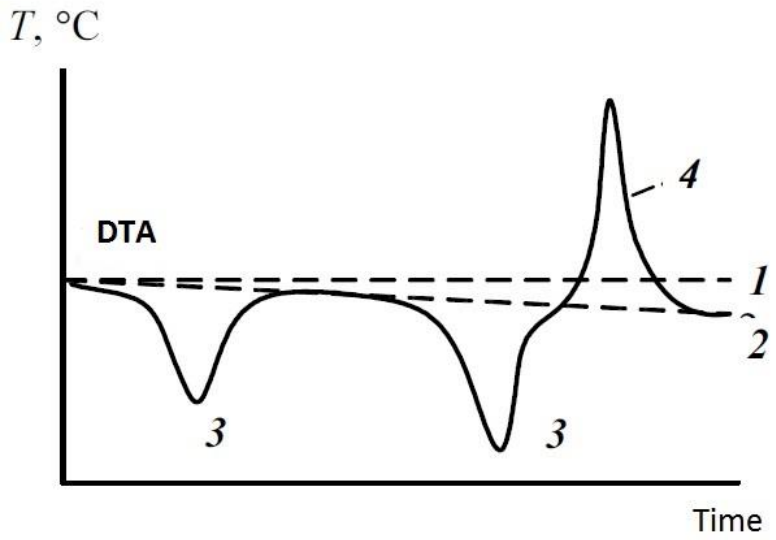

Figure 12. Example of DTA curve: (1) zero line, (2) baseline, (3) endoeffects, (4) exoeffect.

straight line and is called the zero line. If the investigated substance differs from the standard in terms of thermophysical properties, the differential recording curve may deviate from the zero position up or down and be at an angle to the abscissa axis. This line of motion of the thermal curve is called the baseline.

Thermal effects, which are recorded on the DTA curve as deviations below the baseline, are endothermic, and those associated with heat generation and characterized by a deviation of the DTA curve upward are exothermic.

The amplitude of the deviation of the curve from the zero line is an indicator of the intensity of the thermal process. The area of the thermal effect on the DTA curve is directly proportional to the thermal effect of the transformation and inversely proportional to the coefficient of thermal conductivity of the sample. The shape of the endo-and exoeffects on the DTA curves depends on the heating rate-with slow heating, they turn out to be rounded and wide and, with a quick heating, - sharp ones. In most substances, several transformations occur during heating. These are displayed on the DTA curve at the appropriate temperatures by the thermal effects characteristic of the substance. This individual thermal characteristic of the substance reflects its behavior when heated. Thus, according to the thermogram, it is possible to obtain a qualitative characteristic of the sample under study.

The results of thermal analysis are influenced by the following factors:

1) the difference in the thermophysical properties of the reference and test substances (thermal conductivity, thermal diffusivity, and heat capacity). This leads to a deviation of the zero line up (with greater thermal conductivity of the substance under study) or down (with a higher specific heat). Corollary - distortion of the form of the thermal effect, difficulty in determining the temperature;

2) mass and ratio of samples of the test substance and standard. When their thermophysical properties are close to one another, the weights should be the same;

3) the heating rate, especially in the case of slow processes, the imposition of thermal effects;

4) medium in the furnace (neutral, oxidizing and reducing). It can have a significant effect on the nature of the DTA curves, if the processes under investigation are accompanied by mass losses. For example, the onset and duration of dehydration reactions depend on the partial pressure of water vapor. During thermal analysis of substances that are oxidized during heating,

it is necessary to observe a uniform oxidation state. The required medium in the furnace is created by injecting the appropriate gas into it.

5) the granulometric composition of the sample (the fineness of the grinding should be 4000-6000 cm^2/g).

Qualitative analysis of the phase composition of substances and materials using the DTA method is carried out on the basis of known thermographic characteristics of processes: dehydration temperatures; decomposition of carbonates; phase transformations, and so on.

2.5.2. Thermogravimetric analyses (TGA)

Thermogravimetric analysis (TG) makes it possible to determine the changes in mass that occur in the sample when heated. When carrying out the TG, an automatic recording of the change in the mass of the sample is performed depending on the temperature or time.

In practice, the DTA and TG methods are combined, which allows for a comprehensive assessment of the processes occurring. At the same time, the DTG curve (differential-thermogravimetric curve), which records the rate of change in the mass of the substances (the rate of the process) can be recorded. Quickly following one after the other processes, which are superimposed on the thermogravimetric curve, sharply divide on the differential-thermogravimetric curve.

Fig. 13 shows the TG, DTG and DTA curves of dolomite. As seen in this figure, it is possible to obtain information on the temperature intervals for the decomposition of $MgCO_3$ and $CaCO_3$, as well as mass losses associated with decarbonization processes (Papko et al., 2013).

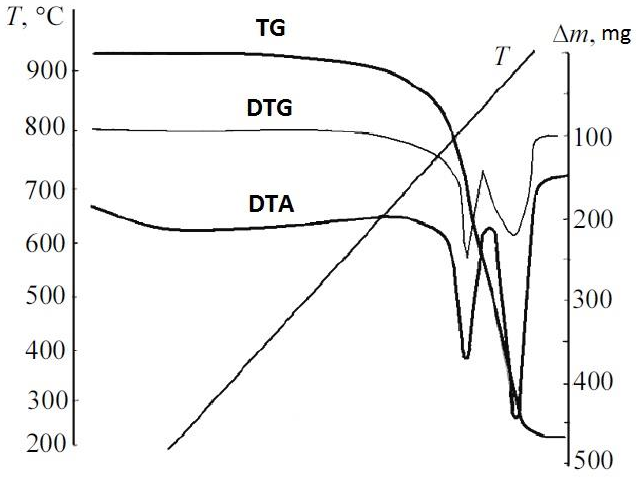

Figure 13. TG, DTG and DTA curves of dolomite.

2.6. Optical emission spectrometry with inductively coupled plasma (ICP-OES)

Optical emission spectrometry with inductively coupled plasma, also called atomic-emission spectrometry with inductively coupled plasma, is an analytical method designed to determine the small contents of a number of elements in samples of various types. This method is a kind of emission spectrometry in which a high-temperature plasma controlled by means of an electromagnetic field is used to excite atoms.

2.6.1. Atomic-emission spectrometry

The emission method of analysis is based on the ability of atoms in an excited state to emit light. Electrons in atoms that have received a sufficient amount of energy - for example, thermal energy - transfer to higher energy levels, and the reverse transition is accompanied by the release of energy in the form of electromagnetic radiation. The atom of each element radiates on strictly defined wavelengths characteristic for a given element, i.e. each element has its own characteristic spectrum. The spectrum of each element has a band of maximum intensity, which corresponds to the most probable electronic transition in an atom. As a rule, different elements have maxima at different wavelengths, and therefore to detect an element in the sample it is sufficient to determine whether the spectrum contains radiation of the appropriate wavelength. Sometimes, however, the lines can overlap. The simplest solution in this case is to take the next in intensity non-overlapping spectral line.

To quantify the content of an element, it is sufficient to measure the radiation intensity at the appropriate wavelength and use a calibration curve to calculate the concentration.

Excitation of atoms can be carried out in various ways. The classical method is the use of a flame of gases such as hydrogen, methane or acetylene in oxygen or purified air. However, this approach has a number of significant drawbacks, the main of which are the instability of the flame, which reduces the reproducibility and accuracy of the results, and the possibility of the formation of oxides, carbides, nitrides, and other highly stable compounds in the flame, which results in distortion of the results.

2.6.2. Inductively coupled plasma

The use of inductively-coupled plasma allows avoiding these problems. In this embodiment, a partially ionized inert gas (usually argon) is used to form a stable high-temperature plasma.

A typical ICP-OES device consists of two parts (Figure 14). The first is a plasma torch in which the atoms of the sample are excited. The second is an optical spectrometer that captures, separates and analyzes the radiation coming from the plasma. The plasma torch consists of three concentric quartz tubes. Around these tubes, the windings of the waveguide are placed, to which an alternating current is fed at a frequency corresponding to the radio frequency electromagnetic region. This current, passing through the windings, creates a powerful electromagnetic field, through which the plasma is maintained and controlled.

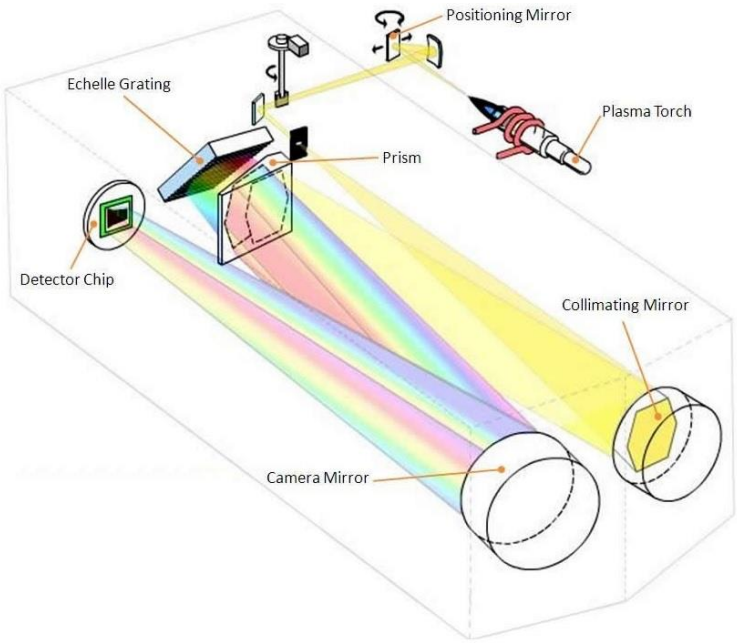

Figure 14. Scheme of ICP-OES device.

To convert the current of argon into plasma, an initial "ignition" is required. For this purpose, an arc or spark high-voltage discharge is passed through the gas, which leads to partial ionization. In turn, charged particles, vigorously colliding with neutral atoms under the influence of electromagnetic oscillations, create new ions. After reaching a certain stable concentration of ionized atoms in the flare, this concentration is further maintained independently. The presence of charged particles in the plasma allows it to interact with the electromagnetic field and to obtain from it sufficient energy to heat the torch to 7000 Kelvin.

Using a peristaltic pump, the sample to be analyzed, in the form of an aqueous or organic solution, enters the nebulizer, which converts the sample into an aerosol form and feeds directly to the argon plasma. After this, atomization and excitation of the investigated elements takes place, the radiation of which is captured by the optics of the device.

The optical part of the optic-emission spectrometer with inductively coupled plasma differs little from the corresponding part of the ordinary atomic-emission spectrometer. Radiation from the torch is collected and focused, and then falls on a polychromator, which is usually a diffraction grating and serves to separate light along wavelengths. The divided light enters the detector (usually a CCD matrix), from which the signal is amplified and processed by the device or a computer connected to it. Modern software packages for ICP-OES spectrometry allow not only to determine the qualitative and quantitative composition of the sample according to the received signal, but also to take into account the overlapping of individual lines and signal-distorting matrix effects in calculations.

3. Objective of this study

The aim of this work was to develop novel cost-efficient nanocomposites synthesized by "green" methods and test these materials as adsorbents for heavy metal cations (Ni^{2+}, Cd^{2+}, Pb^{2+}), phosphorous (phosphates), and sulfur (sulfates).

In the experimental, part the initial target was to prepare various cellulose based nanocomposites, confirm their structures, and study their adsorption properties. Based on the initial results the most promising materials were selected for further comparison after which one particular structure, cellulose reinforced by magnesium hydroxide, was selected for detailed synthesis optimization and characterization.

During the experimental part, a lot of knowledge and novel research results were obtained from the biopolymer based nanocomposites. All of the obtained results are not presented here and the study under this topic will continue.

4. Materials and methods

4.1.Synthesis of nanocomposites

All the chemicals were of analytical grade and used as received without further purification. All the experiments were performed under air atmosphere.

Materials synthesized and their compositions are presented in Table 1.

Table 1. Chemical composition of the prepared nanocomposites

Material name	**Material composition**
CL-MH	Cellulose-$Mg(OH)_2$
CL-LDH2	Cellulose-$[Mg_{1-x}Al_x(OH)_2]^{x+}[CO_3 \cdot nH_2O]^{x-}$
CL-LDH3	Cellulose-$[Zn_{1-x}Al_x(OH)_2]^{x+}[CO_3 \cdot nH_2O]^{x-}$
CL-LDH4	Cellulose-$[Mg_{1-x}Fe_x(OH)_2]^{x+}[CO_3 \cdot nH_2O]^{x-}$
CL-LDH5	Cellulose-$[Mg_{1-x}Al_x(OH)_2]^{x+}[NO_3 \cdot nH_2O]^{x-}$
CL-LDH6	Cellulose-$[Mg_{1-x}Al_x(OH)_2]^{x+}[Cl \cdot nH_2O]^{x-}$
CL-Fe	Cellulose-$Fe(OH)_3$
CL-Mn	Cellulose-MnO_2

4.1.1. Cellulose solution preparation

The procedure of preparing cellulose solution was conducted as described (Yan & Gao, 2008). NaOH-PEG solution containing 9.00 g of NaOH, 1.00 g of PEG and 90.00 g of deionized water were mixed with certain amount of MCC (1.25 g, 2.50g and 5.00 g) under magnetic stirring during couple of minutes and swelled for 3 h at room temperature. Then the cellulose mixture was cooled down to – 15 °C and kept at this temperature during 12 hours. Obtained frozen cellulose mass was defrosted under intensive agitating and then cellulose solution was obtained for further nanocomposite preparation.

4.1.2. Synthesis of CL-MH nanocomposites

For the preparation of cellulose-MH nanocomposites, the following steps were performed: 26.00 mL of 1 M magnesium chloride solution was slowly dropped to 100 mL of obtained cellulose solution with certain cellulose concentration under magnetic stirring. Obtained slurry was refluxed (Fig. 15) or hydrothermally treated in autoclave at a certain temperature for a certain time. The received product was separated from the solution by centrifugation, washed by 50 vol% water ethanol solution several times until neutral pH was reached and dried at 50 °C for 7 h.

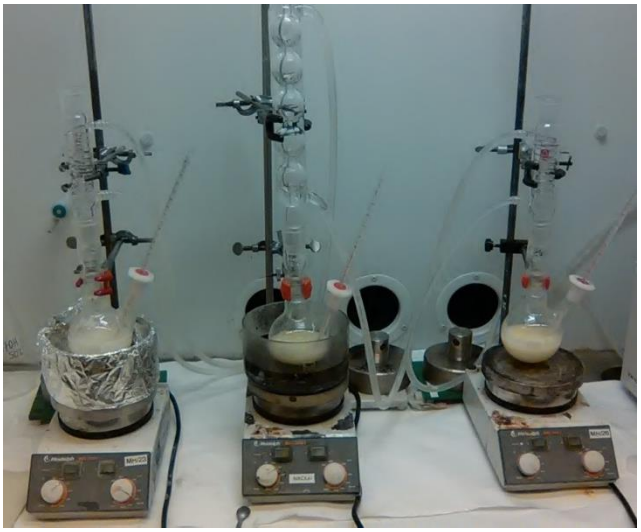

Figure 15. Synthesis of nanocomposites

4.1.3. Synthesis of CL-LDH2 nanocomposites

19.70 mL of 1 M $MgCl_2$ and 4.70 mL of 1 M $AlCl_3$ were mixed. Obtained solution was slowly dropped and 2.0 g of Na_2CO_3 was added to 100 mL of obtained cellulose solution with certain cellulose concentration under magnetic stirring. Obtained slurry was refluxed or hydrothermal

treated in autoclave at a certain temperature for a certain time. The received product was separated from the solution by centrifugation, washed by 50 vol% water ethanol solution several times until neutral pH was reached and dried at 50 °C for 7 h. 10 mL of Na_2CO_3 with concentration 200 g/L was added as carbonate source for interlayer.

4.1.4. Synthesis of CL-LDH3 and CL-LDH4 nanocomposites

Preparation steps of CL-LDH3 and CL-LDH4 materials are absolutely the same, besides used chemicals: $ZnCl_2$ was used instead of $MgCl_2$ for cellulose-$ZnAlCO_3$ and $FeCl_3$ instead of $AlCl_3$ for cellulose-$MgFeCO_3$ respectively.

4.1.5. Synthesis of CL-LDH5 and CL-LDH6 nanocomposites by ion exchange method

1.0 g of fine grinded cellulose –$MgAlCO_3$ was mixed during one night with 0.01 M HNO_3 or HCl to obtain cellulose-$MgAlNO_3$ of cellulose-MgAlCl respectively. The received product was separated from the solution Buchner filtration, washed by 50 vol% water ethanol solution several times until neutral pH was reached and dried at 50 °C for 7 h.

4.1.6. Synthesis of CL-Fe nanocomposite

40 mL of solution containing 8.34 g of $FeSO_4 \cdot 7H_2O$ was slowly dropped into 100 mL of obtained cellulose solution with a certain cellulose concentration under magnetic stirring. After green sludge was formed, the volume of 10 mL of 3% H_2O_2 was slowly dropped. Obtained slurry with a brown color was refluxed at 50 °C. Color changes, which occurred, are shown in Figure 16. The received product was separated from the solution by centrifugation, washed by 50 vol% water ethanol solution for several times until neutral pH was reached and dried at 50 °C for 7 h.

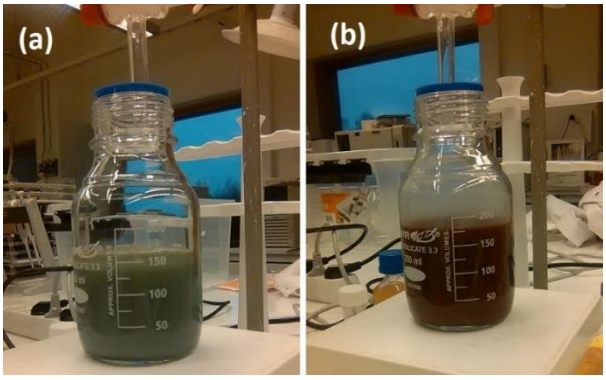

Figure 16. Synthesis steps of CL-Fe nanocomposite: (a) before addition of H_2O_2, (b) after addition of H_2O_2.

4.1.7. Synthesis of CL-Mn nanocomposite

0.474 g of $KMnO_4$ dissolved in 40 mL of water was added to 100 mL of MCC solution. $KMnO_4$ partly reacted with MCC and converted to K_2MnO_4 with characteristic green color. Then 10 mL of 10% H_2O_2 was slowly dropped until color was changed to black, which proved a complete conversion of potassium permanganate and manganate to magnesium dioxide. Also, oxygen from H_2O_2 was released from the mixture during the chemical reaction.

Formation on potassium manganate:

$$KMnO_4 \rightarrow K_2MnO_4 + MnO_2 + O_2\uparrow \quad (6)$$

Formation of manganese oxide (IV):

$$2KMnO_4 + H_2O_2 \rightarrow 2MnO_2 + 2O_2\uparrow + 2KOH \quad (7)$$

Sol was formed, which was proven by Zeta-sizer analyzes. Mixture was allowed to mixed for one night. The received product was separated from the solution by centrifugation, washed by 50 vol% water ethanol solution for several times until neutral pH was reached and dried at 50 °C for 7 h.

However, this method had a significant drawback – MCC reacted with strong oxidizers ($KMnO_4$, H_2O_2). Moreover, this way is not green and was not used for further experiments.

4.2. Adsorption tests

All of listed NC was preliminary tested as adsorbents. Adsorbates were the following ions: Ni, Cd, Pb(II), P (phosphate), S (sulfate). Initial concentration of adsorbates is 0,5 mmol/L. Model solutions of cations were prepared from corresponding nitrates and anions from sodium phosphates and sulfates respectively. Adsorption testes were performed at room temperature, neutral pH, during 1 night in DI water with different adsorbents and adsorbates. Load of adsorbent was 20 mg. Adsorption tests were carried out in 15 mL tubes on orbital shaker. The reaction mixture was filtered using PTFE membranes with pore size of 0,2 micrometers.

4.3. Analytical methods

The crystallinity of products was analyzed by XRD applying PANalytical X-ray diffractometer operating at 40 kV with Co Kα radiation in 2θ range from 10° to 80°. FTIR was performed using a FTIR spectrometer Bruker Vertex 70. SEM images were obtained with a Hitachi S-4800 scanning electron microscope using 30 kV of acceleration voltage, which was equipped

with EDS operated at 30 kV. TEM images were taken with a Hitachi H-7600 transmission electron microscope using 100 kV of acceleration voltage. Thermal decomposition of the cellulose nanocomposite was observed with TGA on a simultaneous thermal analyzer NETZSCH STA 449C at a heating rate of 10 °C min^{-1} from 25 °C to 800 °C.

Concentrations of residual cations and anions after adsorption tests was determined by ICP-OES model iCAP 6300 (Thermo Electron Corporation, USA).

5. Results and discussions

5.1. Characterization of cellulose based nanocomposites

5.1.1. FTIR studies

In order to verify functional groups of materials FTIR studies were performed. Figure 17 shows the composition of some prepared materials.

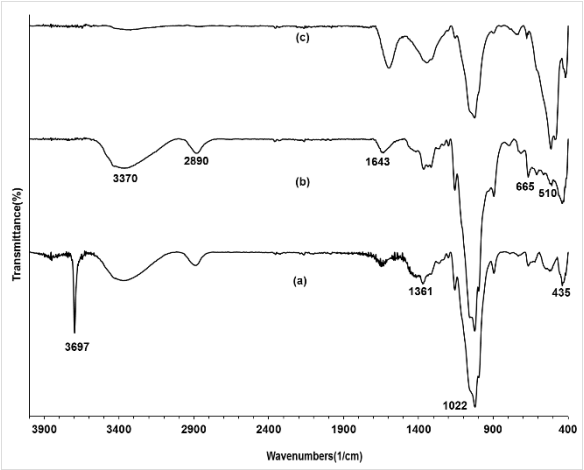

Figure 17. FTIR spectrums of (a) CL-MH, (b) CL-$Fe(OH)_3$, (c) CL-Mn contained prepared at 65 °C for 24 h.

As can be seen from Figure 17 of typical materials, the broad peak at around 3370 cm^{-1} and weak peak at 1643 cm^{-1} belong to OH groups and absorbed water in the all cellulose-MH samples and MCC (Li et al., 2010; Ma et al., 2014). Also a small peak at 1361 cm^{-1} observed for the cellulose based samples can be attributed to OH stretching bonds (Lefatshe et al., 2017) or to "double band to a lowering symmetry of the carbonate" (Cavani, Trifiro, & Vaccari, 1991). The peak at 2890 cm^{-1} corresponding to tension and vibration of C-H in pyranose ring for MCC and cellulose-MH materials. The intense peak at 1022 cm^{-1} and weak peaks at 1155 and 895 cm^{-1} arise from the cellulose in materials. The sharp strong peak at 3697 cm^{-1} corresponds to lattice vibration of $Mg(OH)_2$ (Buchanan, Caspers, & Murphy, 1963) which can be found also in $Mg(OH)_2$ (Fig. 17 (a)) and in all the cellulose-$Mg(OH)_2$ samples. The sharpness and intensity of this peak demonstrate presence of $Mg(OH)_2$ with significant crystallinity for all the samples. In addition, the peaks assigned to vibrations of cations and cation oxygen (M-O and O-M-O) were observed at 200 - 1000 cm^{-1} (Du, Qu, Meng, & Zhu, 2006). For sample of CL-Mn (Fig. 17 (c)) peaks located at 3370 cm^{-1} and 2890 cm^{-1} almost did not exist suggesting decomposition of cellulose during synthesis and making this method unsuitable.

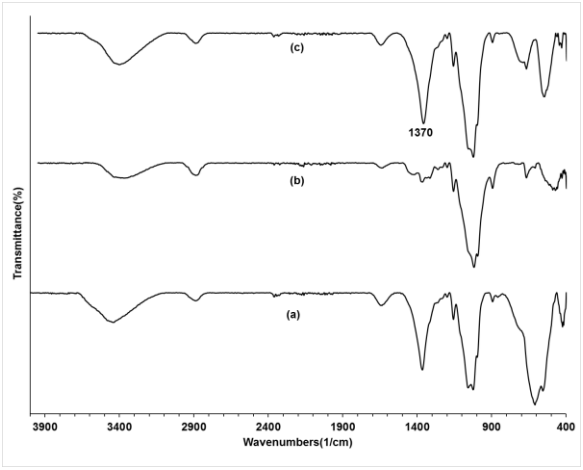

Figure 18. FTIR spectrums of (a) CL-LDH2, (b) CL-LDH3, (c) CL-LDH4 prepared at same conditions.

Figure 18 presents FTIR spectrums of different LDH contained cellulose materials. For CL-LDH2 and CL-LDH4 peaks assigned to carbonates (1370 cm^{-1}) are clearly observed. For CL-LDH 3 carbonate peak is less intensive because of its lower content. Also, peaks in range 400 – 1000 cm^{-1} are different because of different cations of hydroxide layer. According to difference of FTIR spectrums of CL-LDH3, its formation mechanism is different, probably because of amphoteric properties of zinc compared to base properties of magnesium. According to some literature sources (Iftekhar, Srivastava, & Sillanpää, 2017) precise pH control is needed due to significant pH influence on Zn based LDH formation.

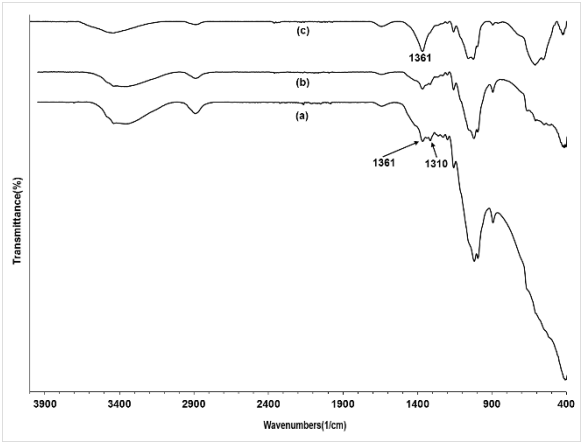

Figure 19. FTIR spectrums of CL-LDH5 and CL-LDH6 prepared from CL-LDH2 by anion exchange method: (a) CL-LDH6, (b) CL-LDH5, (c) CL-LDH2.

Figure 19 shows FTIR spectrums of LDH materials with cellulose matrix prepared by ion exchange method. Carbonate peak at 1361 cm^{-1} is partly substituted by chloride or nitrate anions. Bonded peaks at 1361 cm^{-1} and 1310 cm^{-1} are observed on Figure 19 (a), (b). Peak at 1310 cm^{-1} assigned to nitrate or chloride anion comes from the weak acid. Therefore, substitution of carbonates in interlayer can be confirmed by this method. Also, according to shape of cations related peaks (400 – 1000 cm^{-1}) some structural changes have been occurred due to interaction with weak acid that was applied as a source of anions. Intensity of carbonates or other anions peak is insignificant, that means poor amount of carbonate source in the synthesis. Thus, higher amount of sodium carbonate is needed to optimize the preparation procedure. Moreover, FTIR spectrums of prepared material confirmed previous statement of difficult termination of carbonate anions in LDH materials (Cavani, Trifiro, & Vaccari, 1991). In addition, FTIR spectrums prove substitution of anions and this method is suitable for nanocomposites as well. Further studies are needed to optimize this method for nanocomposites.

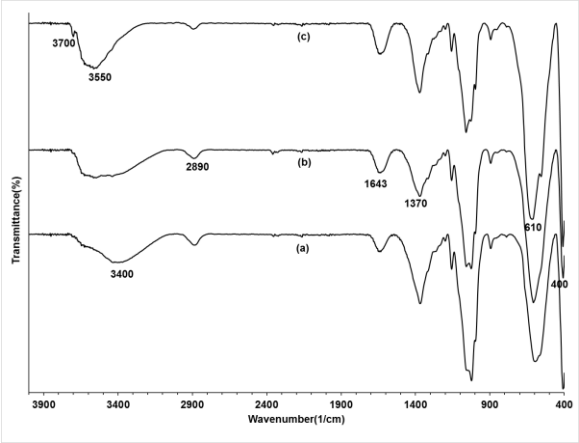

Figure 20. FTIR spectrums of CL-LDH2 material prepared for 24 h at different temperatures: (a) 23 °C, (b) 65 °C, (c) 110 °C in autoclave.

Temperature effect on formation of CL-LDH2 was studied and FTIR spectrums of the samples are shown on Figure 20. Intensity of the peaks assigned to cations in LDH (400 cm^{-1} and 610 cm^{-1}) were increased as a function of process temperature. Also, at 110 °C a small peak at 3700 cm^{-1} assigned to lattice vibration of brucite appeared. Broad peak at 3000-3700 cm^{-1} moved to the left side with increasing temperature. To conclude, temperature influences significantly on the formation of cellulose based LDH nanocomposites.

5.1.2. Structure and morphology studies with TEM

In order to investigate morphology and structure of prepared samples TEM micrographs were made for all the samples.

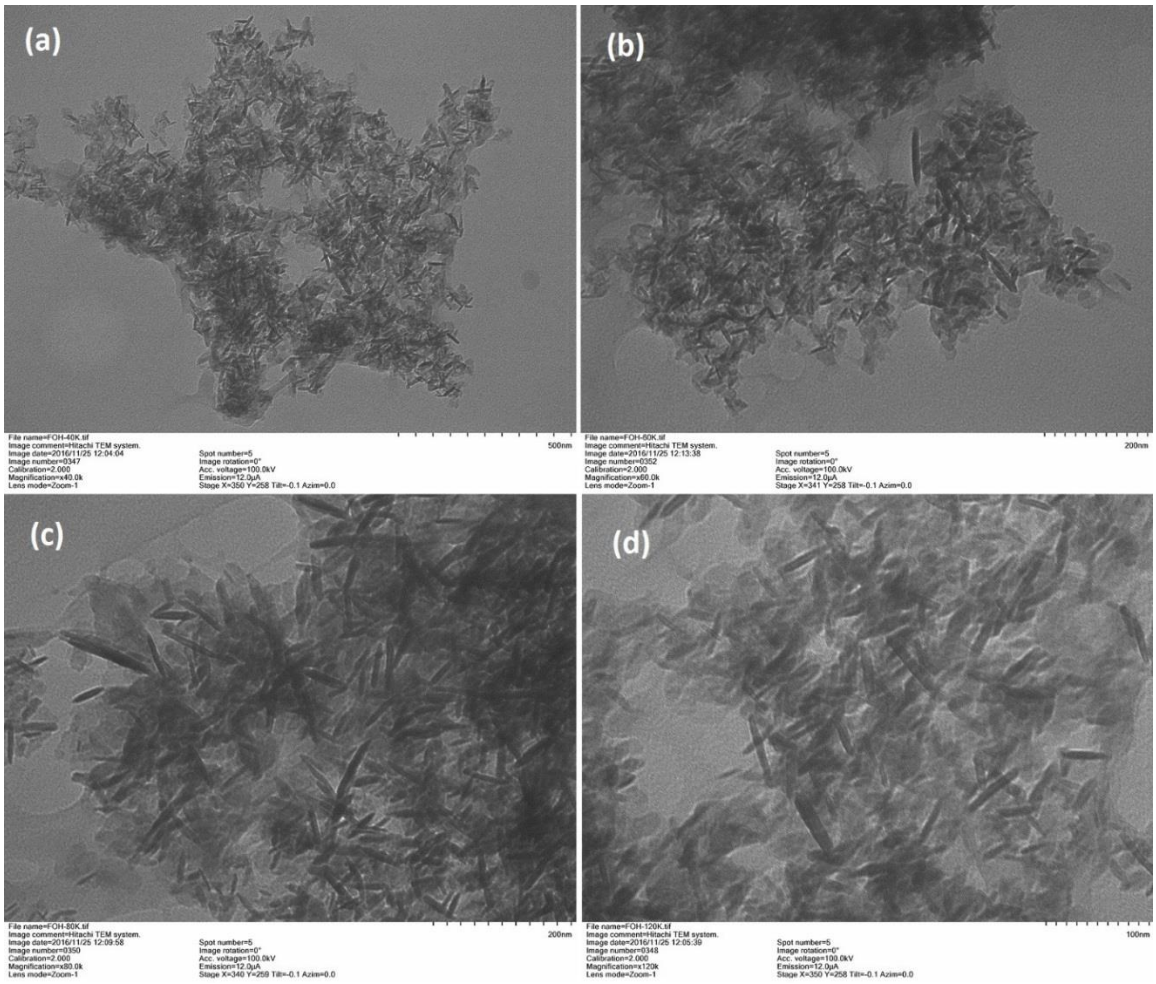

Figure 21. TEM images of CL-Fe sample prepared at room temperature for 24h with various magnification: (a) 40k, (b) 60k, (c) 80k, (d) 120k.

TEM micrographs of cellulose-$Fe(OH)_3$ sample are shown in Figure 21. Nanorods are clearly observed. The length does not exceed 100 nm and the width is 6-10 nm. Nanostructures of reinforcement is evenly distributed in cellulose matrix. Agglomeration of crystals is not significant and particles are mainly separated. Therefore, one of the main drawback of nanoparticles is not observed in CL-Fe nanocomposite. TEM proves that the structure of CL-Fe sample corresponds to nanocomposite.

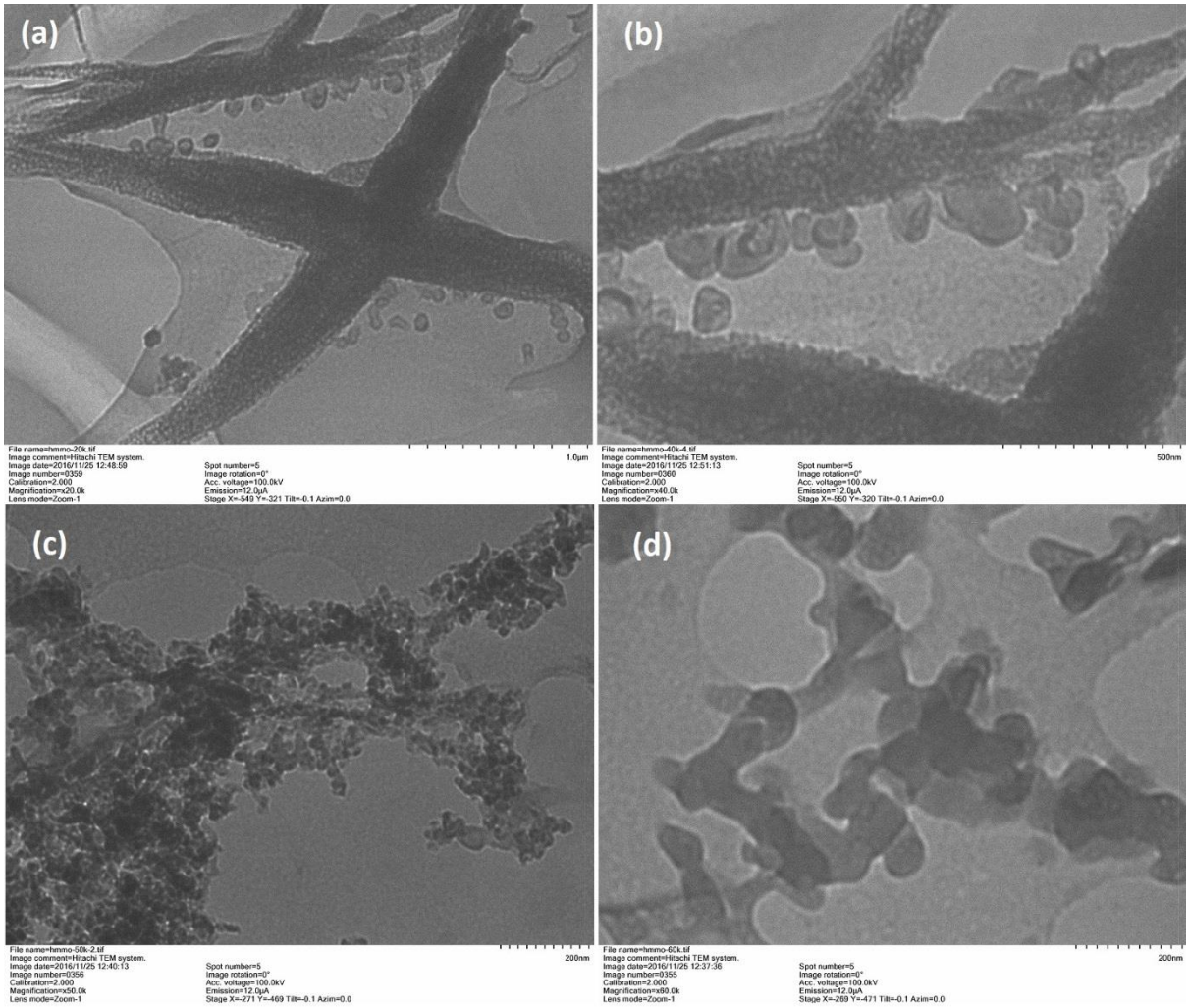

Figure 22. TEM micrograph of CL-Mn samples prepared at room temperature for 24 h with various morphology of nanostructures: (a), (b) spherical particles attached to cellulose fiber; (c), (d) spherical crystals with different size.

Figure 22 (a), (b) shows attached nanostructures to cellulose fibers. The size of attached particles is located in nanorange, approximately 60 nm. Also, spherical crystals with smaller size are clearly observed on micrograph Fig. 22 (c) with size of 15-40 nm. Fig. 22 (d) shows separated nanostructures with average size of 60 nm. According to TEM images cellulose-MnO_2 sample has structure corresponding to nanocomposite. Unfortunately, in accordance to FTIR results cellulose composition has been significantly modified that probably reduced durability of nanocomposite.

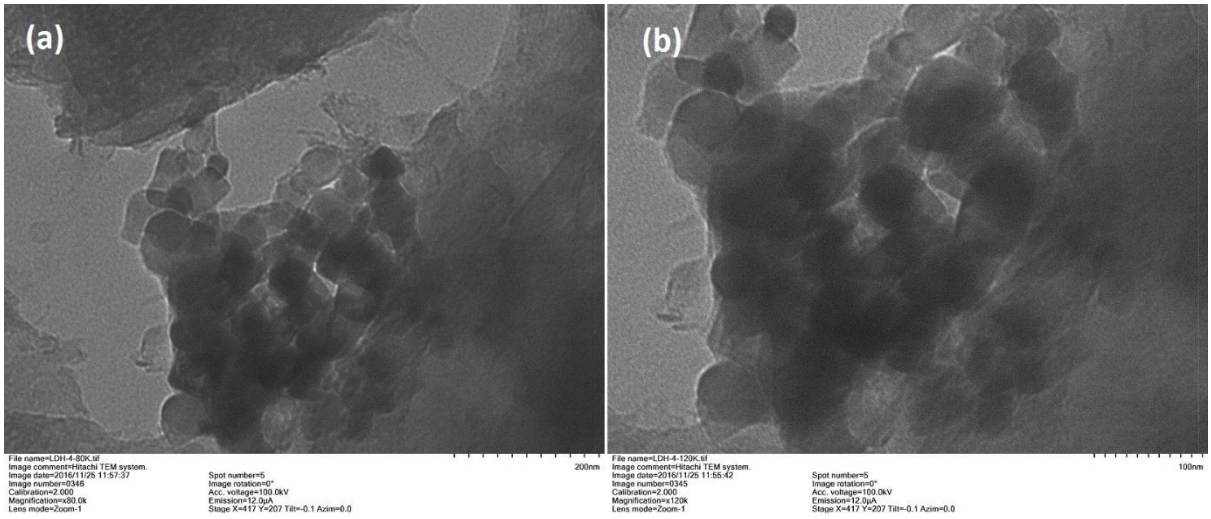

Figure 23. TEM image of CL-LDH4 sample prepared at room temperature for 24 h with two magnifications (a) 80 k; (b) 120 k.

TEM micrograph (Fig.23 (a), (b)) of CL-LDH4 represents two morphology of crystals – cubic and spherical. The size of cubic particles is 40-50 nm and for spherical particles is 25-50 nm. Nanostructures are well distributed in polymer matrix and quite separate. TEM images of CL-LDH4 sample show structure of nanocomposite.

In order to evaluate temperature effect on morphology of samples CL-LDH2 were prepared at room temperature (Fig. 24 (a)), refluxed at 65 °C (Fig. 24 (b)) and hydrothermally treated at 110 °C in autoclave (Fig. 24 (c), (d)). Different types of treatments were performed in order to evaluate influence of temperature and pressure on the composition and structure. Composition has been already discussed in FTIR section. Figure 24 (a) shows integrated agglomerations of nanostructures in cellulose matrix. Crystal size is 30-50 nm. Nanostructure are quite agglomerated in CL-LDH2 sample prepared at room temperature. Even distribution is observed for CL-LDH2 sample refluxed at 65 °C (Fig. 24 (b)). Also, crystal size is larger compared to sample prepared at 23 °C. Moreover, with increasing of temperature nanorods were appeared. Figure 24 (c), (d) shows CL-LDH2 sample prepared by hydrothermal treatment at 110 °C. We can see evenly distributed, non-agglomerated nanostructures with two morphology types. Compared to refluxed samples spherical particles do not dominate in the sample. Presence of nanorods is almost equal in all samples. TEM micrographs shows even distribution for nanoparticles of samples prepared at higher than room temperature. Otherwise, even for sample prepared at 23 °C nanocomposite structure was observed. Therefore, temperature had a clear influence on the morphology and composition of the materials but according to Figure 24 (c),

(d), pressure did not affect this notably. For further studies temperature was varied only by simple refluxing that has been described in materials and method section.

According to TEM micrographs, all the cellulose based materials have structure corresponding to nanocomposite and the temperature significantly effects on the structure and morphology of the samples. Cellulose-$Mg(OH)_2$ materials will be discussed in more detailed in the next sections.

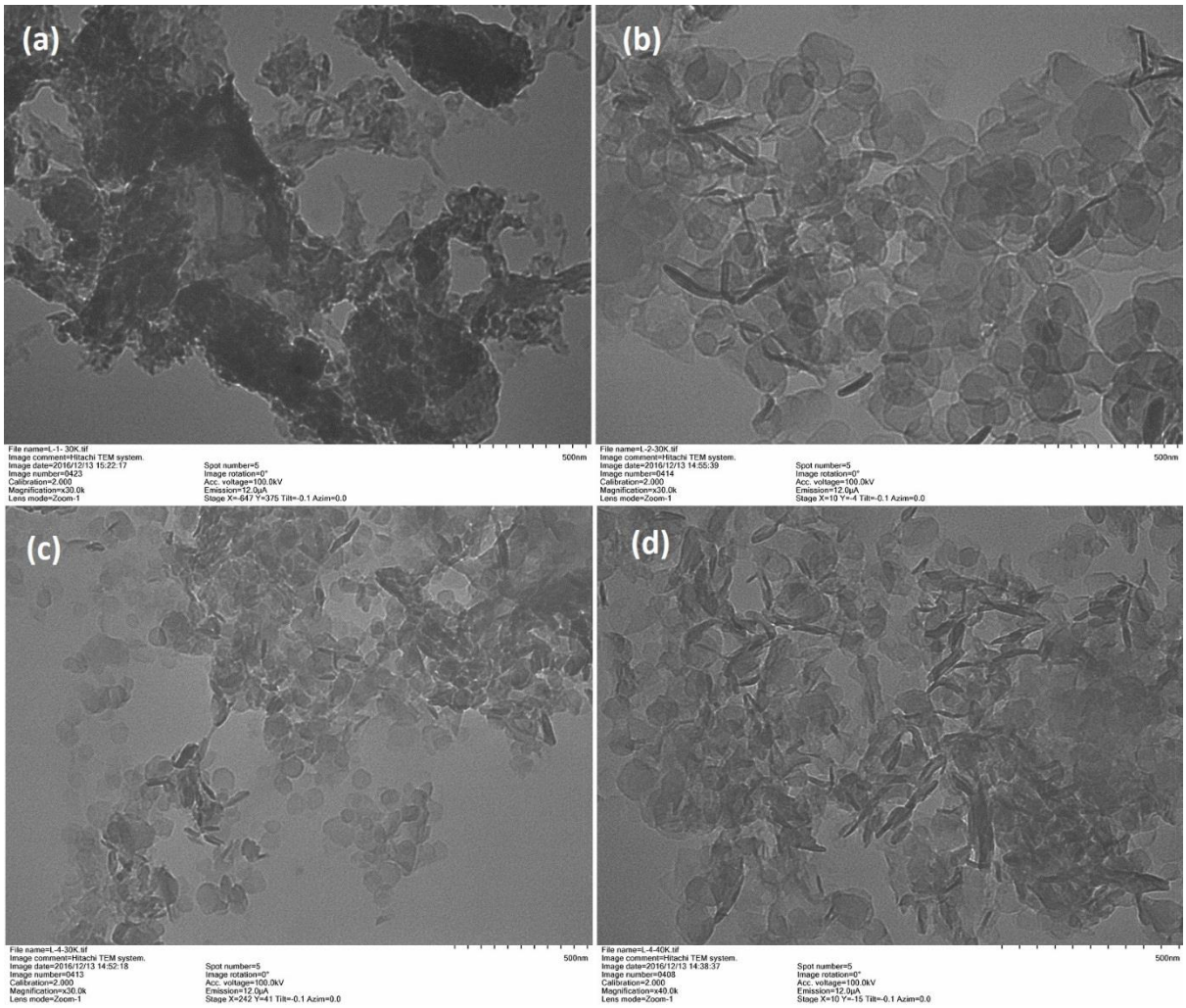

Figure 24. TEM images of CL-LDH2 samples prepared for 24h at different temperature: (a) 23 °C; (b) 65 °C; (c), (d) 110 °C in autoclave.

5.2. Adsorption tests

To evaluate adsorption performance of each material, preliminary adsorption tests were performed. Cellulose based materials reinforced by LDHs, MnO_2, $Fe(OH)_3$ and $Mg(OH)_2$ were tested. Only preliminary results, which represent removal degree of pollutants was obtained. However, results are sufficient to evaluate adsorption possibility for the further studies.

5.2.1. Adsorption results of cellulose-based materials reinforced by LDH

The following materials were tested (Table 2). Materials were various LDHs with different hydroxide layer (Mg^{2+}or Zn^{2+} as divalent cation and Al^{3+} or Fe^{3+}as trivalent anion) and different interlayers: CO_3^{2-}, NO_3^{2-} and Cl^{-}.

Table 2. Composition of cellulose based adsorbents reinforced by LDH

Adsorbent	**Reinforcement**
CL-LDH2	$[Mg_{1-x}Al_x(OH)_2]^{x+}[CO_3 \cdot nH_2O]^{x-}$
CL-LDH3	$[Zn_{1-x}Al_x(OH)_2]^{x+}[CO_3 \cdot nH_2O]^{x-}$
CL-LDH4	$[Mg_{1-x}Fe_x(OH)_2]^{x+}[CO_3 \cdot nH_2O]^{x-}$
CL-LDH5	$[Mg_{1-x}Al_x(OH)_2]^{x+}[NO_3 \cdot nH_2O]^{x-}$
CL-LDH6	$[Mg_{1-x}Al_x(OH)_2]^{x+}[Cl \cdot nH_2O]^{x-}$

Results of adsorption tests are shown in Table 3 and on Figure 25.

Table 3. Adsorption results of cellulose based materials reinforced by LDHs.

Reinforcment	**Adsorbate**	**Initial concentration, Cin [ppm]**	**Final concentration, Cf [ppm]**	**pHfinal**	**Uptake, %**
CL-LDH2	Ni	30.93	0.32	6.27	98.98
	Cd	65.60	1.38	3.37	97.89
	Pb	111.76	0.09	3.14	99.92
	S	18.48	15.54	6.40	15.91
	P	18.45	12.08	4.05	34.54
CL-LDH3	Ni	30.03	27.50	3.43	8.43
	Cd	63.75	59.53	3.31	6.62
	Pb	106.66	54.20	3.25	49.19
	S	18.43	19.04	3.36	0.00
	P	19.08	4.58	2.97	75.99
CL-LDH4	Ni	30.15	0.08	3.41	99.75
	Cd	63.51	0.70	3.24	98.90
	Pb	106.66	0.34	3.72	99.69
	S	19.06	14.12	3.80	25.88
	P	19.15	13.07	3.72	31.78
CL-LDH5	Ni	29.87	11.52	4.45	61.42
	Cd	63.57	37.18	3.89	41.51
	Pb	106.93	54.32	3.58	49.20
	S	18.70	15.27	3.80	18.34
	P	19.05	8.34	3.80	56.25
CL-LDH6	Ni	29.46	14.65	3.89	50.26
	Cd	63.93	48.38	3.91	24.32
	Pb	107.62	29.49	3.60	72.60
	S	19.52	15.16	3.90	22.33
	P	19.11	12.25	3.81	35.91

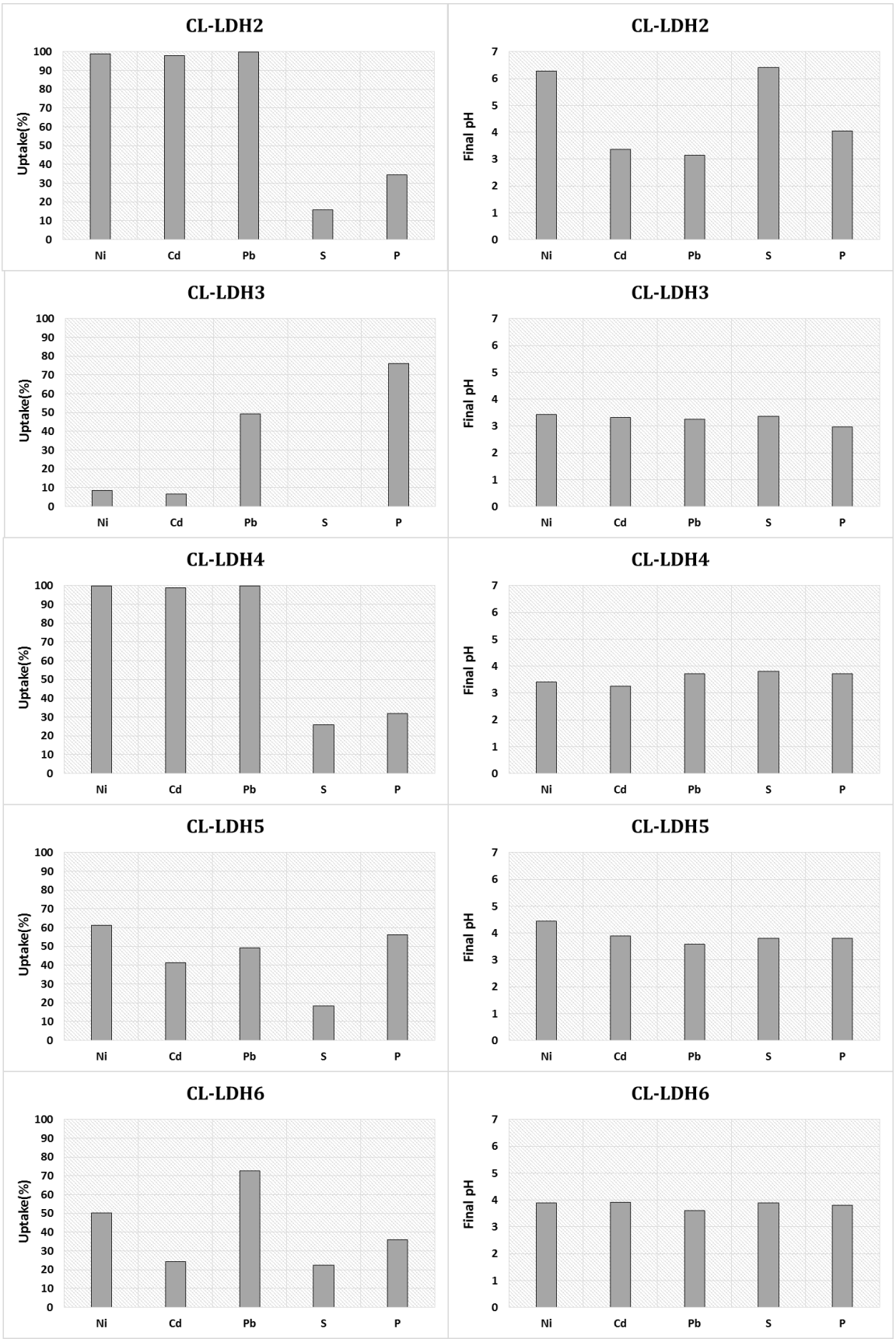

Figure 25. Graphical representation of adsorption results of CL-LDHs materials.

According to the adsorption results of LDH reinforced materials, samples LDH2 and LDH4 have excellent adsorption performance for cations compared to other samples. Sample CL-LDH5 (modified CL-LDH2) shows quite stable uptake of both cations and anions. The best adsorbents for cations are magnesium contained samples. Therefore, it can be concluded that magnesium significantly effects on the adsorption performance. Instead of LDH, only magnesium contained composites were further investigated because of their feasibility compared to LDH. Futhermore, brucite has the same structure than LDH and probably will demonstrate a similar adsorption behavior. Accordingly, sample CL-$Mg(OH)_2$ was prepared and studied in next sections with the other materials.

After adsorption pH was decreased, which can be explained by the adsorption mechanism: adsorption/surface complexation, isomorphic substitution, precipitation and surface complexation (Liang et al., 2013), Fig. 26.

Metal cation adsorption can be explained by the chemical reactions (Liang et al., 2013):

$$\text{Sur-OH} + M^{2+} \rightarrow \text{Sur-O-}M^{+} + H^{+} \quad (8)$$

$$\text{Sur-OH} + MOH^{+} \rightarrow \text{Sur-O-}M^{+} + H_2O \quad (9)$$

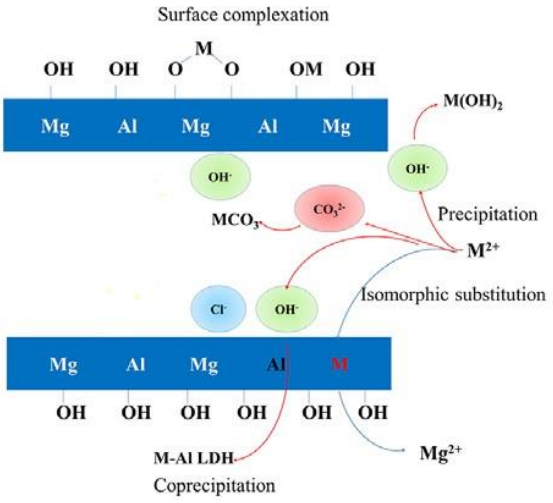

Figure 26. Adsorption mechanism of LDH materials (Liang et al., 2013).

Formation of inner-sphere complexes and outer-sphere complexes can occur by interaction with surface hydroxyl groups of LDH and deprotonated hydroxyl groups (Sur-O^{-}) respectively (Deng, Zhang, Cui, Shi, & Deng, 2011):

$$\text{Sur-O}^{-} + Pb^{2+} \rightarrow \text{Sur-O}^{-}\ldots Pb^{2+} \quad (10)$$

$$Sur\text{-}O^- + Cd^{2+} \rightarrow Sur\text{-}O^-\ldots Cd^{2+} \quad (11)$$

$$Sur\text{-}OH + Cd^{2+} \rightarrow Sur\text{-}O\text{-}Cd^{+} + H^{+} \quad (12)$$

Isomorphic substitution is an exchange of element or group of elements (compounds) in LDH which are not placed in crystal structure. Size and charge of substituted ions should be the same (Liang et al., 2013). The process can be explained by the reaction:

$$[Mg_3Fe(OH)_8]^{+} + Pb^{2+} \rightarrow [Mg_3Fe(OPb)(OH)_7]^{2+} + H^{+} \quad (13)$$

In fresh prepared LDH divalent metals can be substituted even in hydroxide layer with formation of product with composition of $[M^{2+}Mg]_2Al(OH)_6Cl$ (Liang et al., 2013).

According to mentioned reactions decrease of the pH can be explained by liberation of proton H^+. However, precipitation is possible simultaneously with these reactions if the pH is increased:

$$4Pb^{2+} + 2Cl^- + 6OH^- \rightarrow Pb_3(OH)_6PbCl_2 \rightarrow Pb_4O_3Cl_2 + H_2O \quad (14)$$

$$3Pb^{2+} + 2CO_3^{2-} + 2OH^- \rightarrow Pb_3(CO_3)_2(OH)_2 \quad (15)$$

All of the mentioned mechanisms are possible and fair in our case. A number of articles have been published related to adsorption mechanism of LDH (Liang et al., 2013; Park et al., 2007). However, more detailed studies are needed to estimate influence for each mechanism in the present case. Anyway, mentioned phenomena is true for cellulose based materials reinforced by LDH because cellulose has insignificant adsorption performance compare to reinforcement (LDH). It is important to note that the mentioned mechanisms are also applied for the cellulose based materials reinforced by brucite because brucite has the same structure as LDH except of absence of trivalent cations in hydroxide layers. Existing difference does not significantly effect on the adsorption mechanisms.

5.2.2. Adsorption results of cellulose-based materials reinforced by $Mg(OH)_2$, $Fe(OH)_3$ and MnO_2

As was explained in previous chapter, brucite reinforcement could be checked as a potential reinforcement agent. Also, for further comparison of the adsorption properties, iron oxide (III) manganese oxide (IV) and mixed iron oxide contained materials were prepared and tested (table 4).

Table 4. Composition of cellulose based adsorbents reinforced by metal oxides and hydroxides

Adsorbent	**Reinforcement**
CL-MH	$Mg(OH)_2$ - brucite (magnesium hydroxide)
CL-Fe	$Fe(OH)_3$ - iron hydroxide (III)
CL-Mn	MnO_2 - manganese oxide (III)
CL-Fe3O4	Fe_3O_4 - mixed iron oxide

In the case of Fe_3O_4, commercial nano powder of mixed iron oxide was dispersed in cellulose solution by intensive stirring. Fe_3O_4 was not obtained in situ.

Results of adsorption tests are shown below in Table 5 and on Figure 27.

Table 5. Adsorption results of cellulosed based materials with different reinforcments

Reinforcment	**Element of adsorbate**	**Initial concentration, Cin [ppm]**	**Initial concentration, Cf [ppm]**	**pHfinal**	**Uptake, %**
CL-MH	Ni	32.71	0.01	5.29	99.96
	Cd	65.84	0.15	4.90	99.78
	Pb	112.50	1.01	3.73	99.10
	S	21.24	20.21	7.11	4.84
	P	21.15	10.25	7.73	51.55
CL-Fe	Ni	32.71	16.54	3.49	49.44
	Cd	65.84	36.16	3.50	45.07
	Pb	112.50	32.55	3.21	71.07
	S	21.24	20.68	4.17	2.64
	P	21.15	14.97	5.70	29.21
CL-Mn	Ni	32.71	0.08	6.40	99.74
	Cd	65.84	0.22	5.81	99.66
	Pb	112.50	2.26	6.10	97.99
	S	21.24	20.93	9.51	1.47
	P	21.15	21.15	7.48	0.00
CL-Fe3O4	Ni	32.71	29.94	3.39	8.48
	Cd	65.84	61.89	3.34	6.00
	Pb	112.50	97.76	3.34	13.10
	S	21.24	20.71	3.44	2.51
	P	21.15	19.54	3.50	7.63

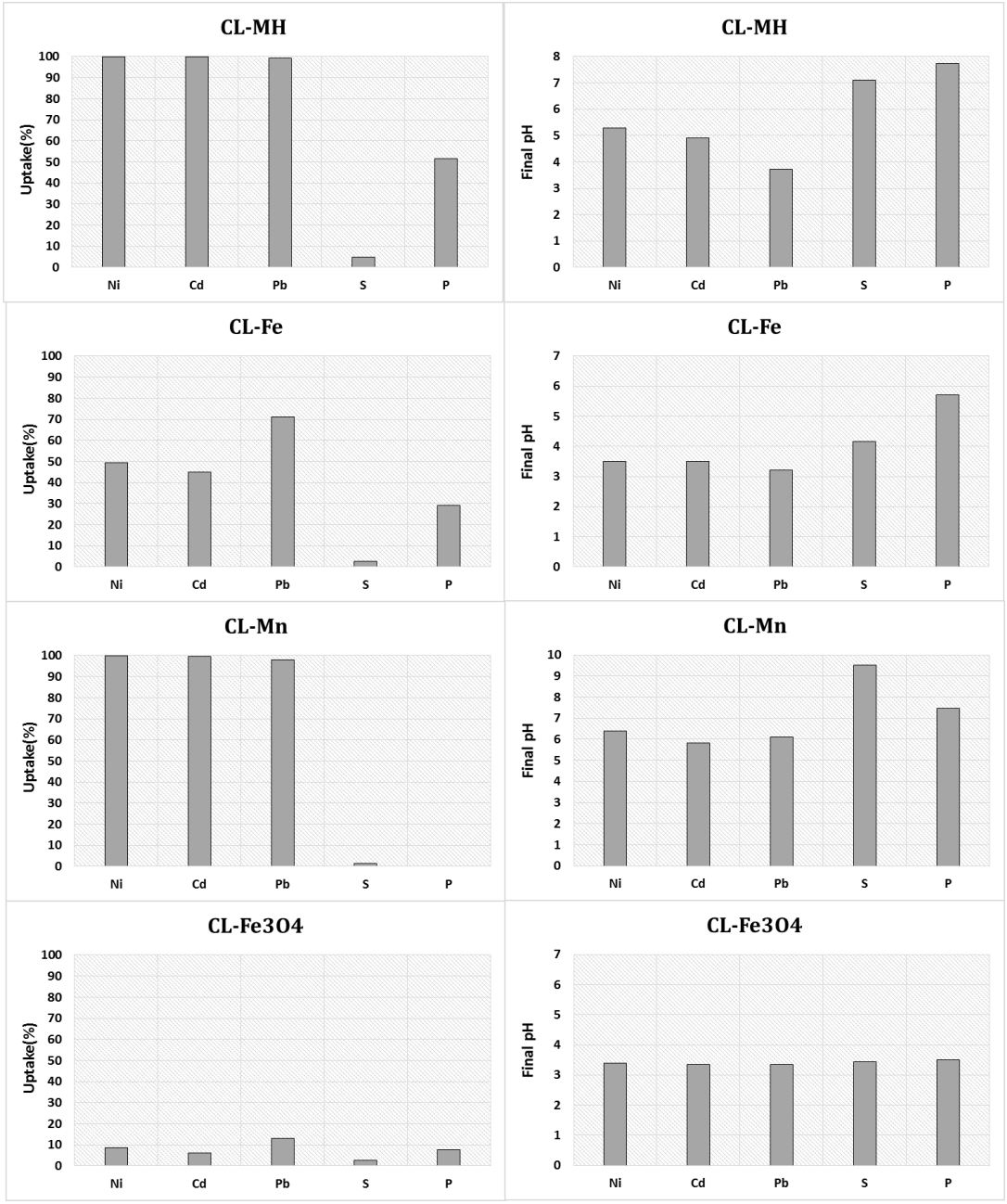

Figure 27. Adsorption results and final pH of second adsorption test

According to the second results, suggestion that Mg^{2+} significant influences on adsorption performance has been further confirmed because Mg contained samples showed an excellent adsorption performance. This is because Mg^{2+} is effectively exchanged with metal cations Me^{2+}. Confirmation of exchange mechanism will be further discussed.

Also, good adsorption of phosphorous and satisfied for sulphur was observed. Manganese contained composite showed excellent adsorption for cations, but did not work with anions. Iron (III) hydroxide worked satisfactorily for cations. Mixed Fe_3O_4 oxide almost did not work.

To confirm ion exchange mechanism some adsorption tests were repeated and magnesium concentration was determined. Uptake of heavy metal cations was the same. Results are shown in Table 6.

Table 6. Concentration of magnesium Mg^{2+} after adsorption test of CL-MH

Element of adsorbate	**Initial concentration, Cin [ppm]**	**Final concentration, Cf [ppm]**	**Liberated Mg^{2+} concentration, CMg [ppm]**	**Uptake, %**
Ni	30.70	0.03	29.36	99.91
Cd	59.74	0.19	28.04	99.68
Pb	105.25	0.29	27.39	99.72
S	19.82	19.76	21.65	0.28
P	18.23	8.02	24.48	56.00

According to Table 6, presence of magnesium in the solution after adsorption was observed. Magnesium comes from brucite due to some chemical reactions, which were described above (see adsorption mechanism section). Therefore, ion exchange mechanism of adsorption by Mg containing materials can be verified.

5.3. Material selection for further studies

According to mentioned results there are the following materials with structure corresponding to nanocomposites CL-LDH2, CL-LDH4, CL-MH, CL-Mn and CL-Fe. Composites CL-Mn and CL-Fe are not considered for further comparison because of the destructive synthesis conditions for cellulose. Cellulose can be modified or destructed by chemicals, which are used in synthesis. This fact provides a number of drawbacks and therefore these two potential adsorbents are not interested despite their good adsorption properties. As a conclusion, CL-LDH2, CL-LDH4 and CL-MH selected for more detailed comparison in Table 7.

Cellulose-$Mg(OH)_2$ material has some significant benefits compared to other studied materials. This is the reason why CL-MH was finally selected for further studies. Cellulose-MH material has sufficient adsorption performance, synthesis of CL-MH is the most cost-efficient, and simple (in other words green, mainly because of one precursor) compared to other prepared and studied materials. Therefore, the next chapters in this work are related to the synthesis of cellulose based nanocomposites reinforced by magnesium hydroxide (brucite) using a green technique.

Table 7. Comparison of materials

Material	**Composition**	**Advantages**	**Drawbacks**
CL-LDH2	$MgAlCO_3$/cellulose	-nanocomposite -various application of intercalated LDH as well as adsorbent and catalyst -satisfactory adsorbs S and P -further modification, change anion part	-this LDH-CL nanocomposite has been already synthesized, but by other method -2 precursors for LDH -quite difficult because LDH
CL-LDH4	$MgFeCO_3$/cellulose	-nanocomposite -this LDH-CL nanocomposite has never been synthesized -satisfactory adsorbs S and P -further modification, change anion part	-2 precursors for LDH -quite difficult because LDH
CL-MH	$Mg(OH)_2$/cellulose	-nanocomposite -this Mg-cellulose based composite has never been synthesized -good adsorbs P (50%) -only 1 precursor -more feasible compare to LDH	-unsatisfied S adsorption

5.4. Studies of cellulose based nanocomposite reinforced with brucite

5.4.1. FTIR studies

In order to verify functional groups of the material FTIR studies were performed. Figure 28 (A) (a-c) shows the comparison of FTIR spectra of synthesized brucite (a), cellulose-MH sample (b) and raw MCC (c). Brucite was prepared in the same manner as cellulose-MH samples without MCC in order to confirm existence of $Mg(OH)_2$ in cellulose based samples. In order to investigate the effect of temperature on cellulose-MH materials, samples were prepared at 23, 65 and 100 °C (Fig. 28 (B) spectrums (d), (e) and (f) respectively).

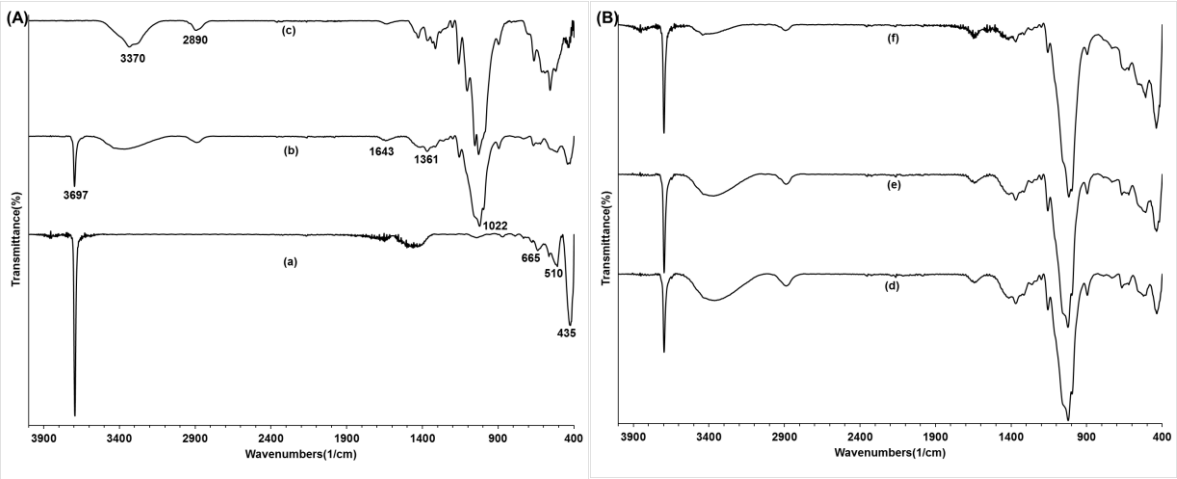

Figure 28. FTIR patterns of (A) (a) brucite; (b) cellulose-Mg(OH)2 nanocomposite; (c) pure MCC and (B) cellulose-Mg(OH)2 nanocomposites prepared for 24 h at different temperatures: (d) 23 °C; (e) 65 °C; (f) 100 °C.

The broad peak at around 3370 cm^{-1} and weak peak at 1643 cm^{-1} belong to OH groups and absorbed water in the all cellulose-MH samples and MCC (Li et al., 2010; Ma et al., 2014). Also small peak at 1361 cm-1 observed for the cellulose based samples can be attributed to OH stretching bonds (Lefatshe et al., 2017) or to "double band to a lowering symmetry of the carbonate" (Cavani et al., 1991). The peak at 2890 cm^{-1} corresponds to the tension and vibration of C-H in pyranose ring of MCC and cellulose-MH materials. The intense peak at 1022 cm^{-1} and weak peaks at 1155 and 895 cm^{-1} arise also from the cellulose in materials. The sharp strong peak at 3697 cm^{-1} corresponds to lattice vibration of $Mg(OH)_2$ (Buchanan, Caspers, & Murphy, 1963) which can be found also in $Mg(OH)_2$ (Fig. 28 (A) (a)) and in all the cellulose-$Mg(OH)_2$ samples. The sharpness and intensity of this peak demonstrate presence of $Mg(OH)_2$ with significant crystallinity for all samples. In addition, the peaks assigned to bending modes

of Mg-O bonds and cellulose were observed at 665 and 510 cm^{-1}. As Figure 28 (B) (d-f) shows that intensities of the peaks ascribed to $Mg(OH)_2$, especially 3697 and 435 cm^{-1}, were increased as a function of the process temperature. The same behavior was observed for peaks at 665 and 510 cm^{-1}. Therefore, temperature has a significant structure effect on the cellulose-MH nanocomposites formation.

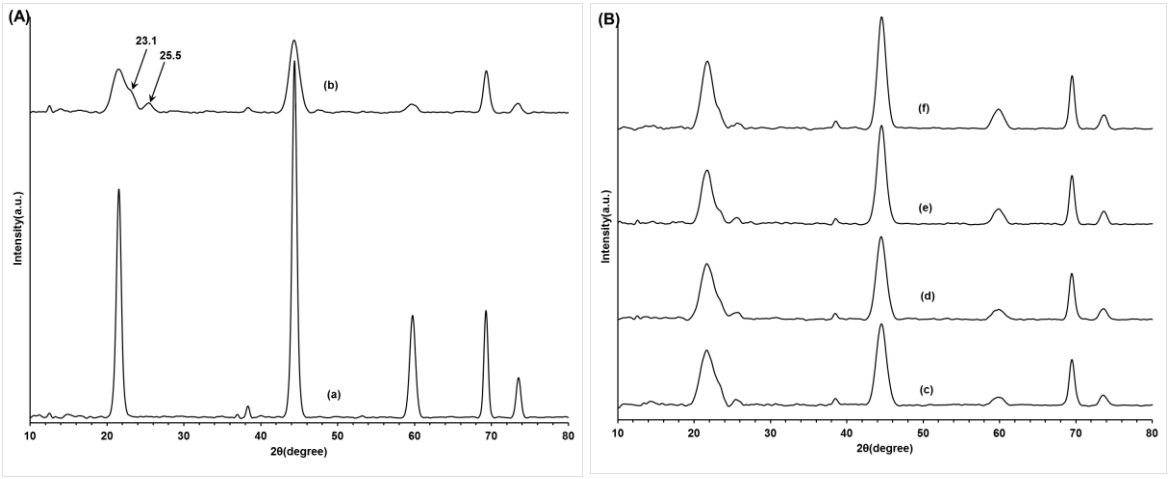

Figure 29. XRD patterns of (A) (a) brucite; (b) cellulose-Mg(OH)2 nanocomposite and (B) cellulose-MH samples prepared at 65 °C for different times: (c) 3 h; (d) 6 h; (e) 12 h; (f) 24 h.

5.4.2. XRD studies

The samples were studied with X-ray power diffraction to evaluate the crystal structure. Figure 29 (A) (a) shows synthesized brucite in situ and a typical cellulose-MH sample (Fig. 29 (A) (b)). The broad peak at around 2θ = 23.1° and peak at around 2θ = 25.5° are assigned to cellulose (Fig. 29 (A) (b)). All other observed diffraction peaks are attributed to the phase of well crystalline brucite (ICSD 98-007-9031). One can see the increase of the peak intensity of $Mg(OH)_2$ phase and decrease peak intensity of cellulose with increasing of heating time, which could be assigned to the interaction between MCC and brucite (Fig.29 (B) (c-f)). Diffraction peaks corresponding to $Mg(OH)_2$ are clear and well distributed, which demonstrate the well crystallized reinforcement phase in cellulose. The average crystal size calculated by using Scherrer equation is 7 -26 nm (Langford & Wilson, 1978). According to FTIR and XRD results, all of the samples produced at different time or temperature have structure corresponding to cellulose-$Mg(OH)_2$ nanocomposites.

5.4.3. TGA and DTA analyses

The thermal stability of cellulose-MH nanocomposites with various MCC amount were studied with thermogravimetry (TG) and differential thermogravimetry (DTG) as shown in Figures 30 (A) and 30 (B). All of the samples have the similar TG and DTG curves. The TGA curve (Fig. 30 (A)) shows a small weight loss at around 100 °C assigned to the desorption of water. Adsorbed water loss is also clearly observed on DTG curve (Fig. 30 (B)). The first significant weight loss around 295-312 °C can be attributed to the thermal degradation of cellulose. The second obvious weight loss at 380-400 °C was caused by complete decomposition of cellulose in nanocomposite. When the cellulose-MH nanocomposite were prepared with decreasing cellulose amount, 1.25 g, 2.50 g and 5.00 g, the total weight losses of 55.6%, 67.2% and 72.6% were occurred accordingly, identifying that the cellulose content in the cellulose-MH nanocomposites reduced with reducing the amount of raw cellulose used in the synthesis.

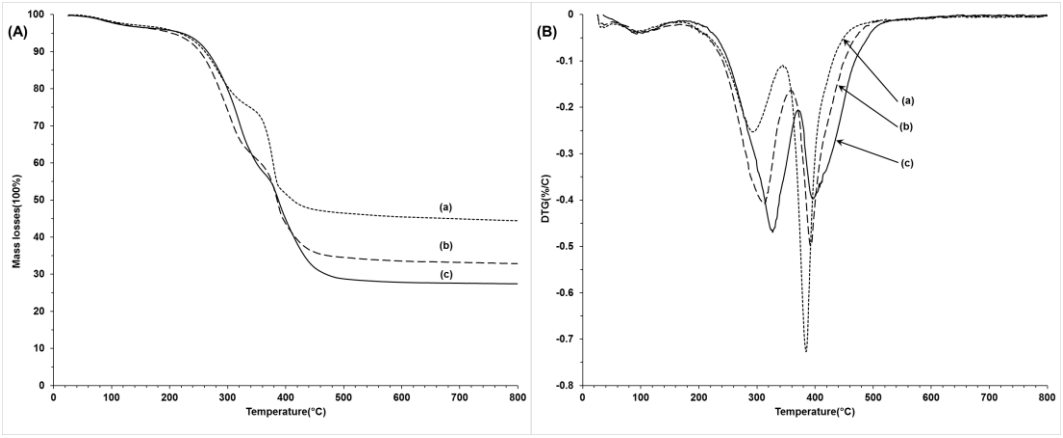

Figure 30. (A) TG and (B) DTG curves of the cellulose-MH nanocomposites using different cellulose amount at 65 °C for 24 h: (a) 1.25 g; (b) 2.50 g; (c) 5.00 g.

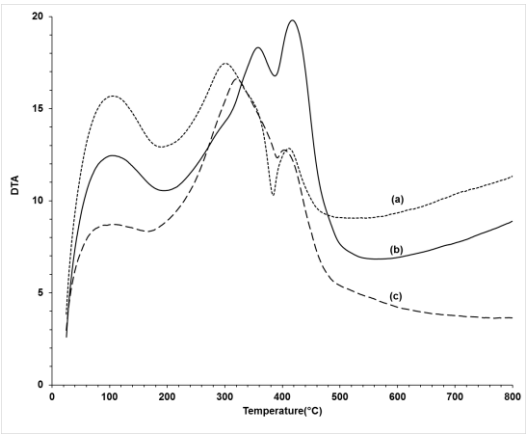

Figure 31. DTA curves of the cellulose-MH nanocomposites using different cellulose amount at 65 °C for 24 h: (a) 1.25 g; (b) 2.50 g; (c) 5.00 g.

Figure 31 shows DTA curve of cellulose-MH samples. Two significant endothermic peaks observed at 295-312 °C and 380-400 °C are attributed to thermal degradation and complete decomposition of cellulose respectively. DTA and DTG peaks locate in the same position that indicate endothermic degradation of cellulose in the certain temperature range.

To confirm the right composition of cellulose-MH nanocomposites with various MCC amount, FTIR studies were performed for samples with 1.25 g, 2.50 g and 5.00 g of MCC content. As can be seen from Figure 32 (a-c), the characteristic peaks of cellulose are increased and peaks of brucite decreased with increasing the amount of cellulose in the samples.

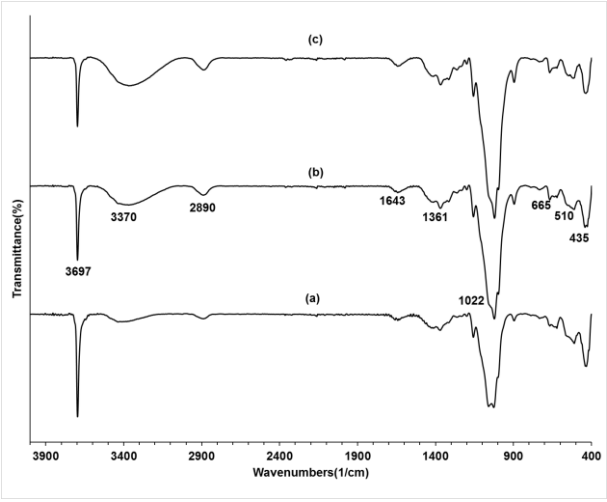

Figure 32. FTIR spectrums of the cellulose-MH nanocomposites using different cellulose content at 65 °C for 24 h: (a) 1.25 g; (b) 2.50 g; (c) 5.00 g.

5.4.4. SEM and TEM studies

In order to investigate the morphology of the samples, cellulose-MH nanocomposites were studied with TEM and SEM. Figure 33 shows a typical sample of cellulose-MH nanocomposite prepared at 65 °C for 24 hours. Three morphology types of magnesium hydroxide were observed. On Figure 33 (a) rod like and hexagonal $Mg(OH)_2$ nanocrystals can be seen and in Figure 33 (b) spherical MH crystals are observed. Also, spherical $Mg(OH)_2$ nanostructures with smaller size are visible in Figure 33 (c). Figure 33 (d) shows embedded brucite particles with cellulose. According to TEM the average crystal size of hexagonal and spherical particles is around 20-50 nm. For rod like crystals the length is a couple of hundreds nanometers and the width approximately 10-30 nm.

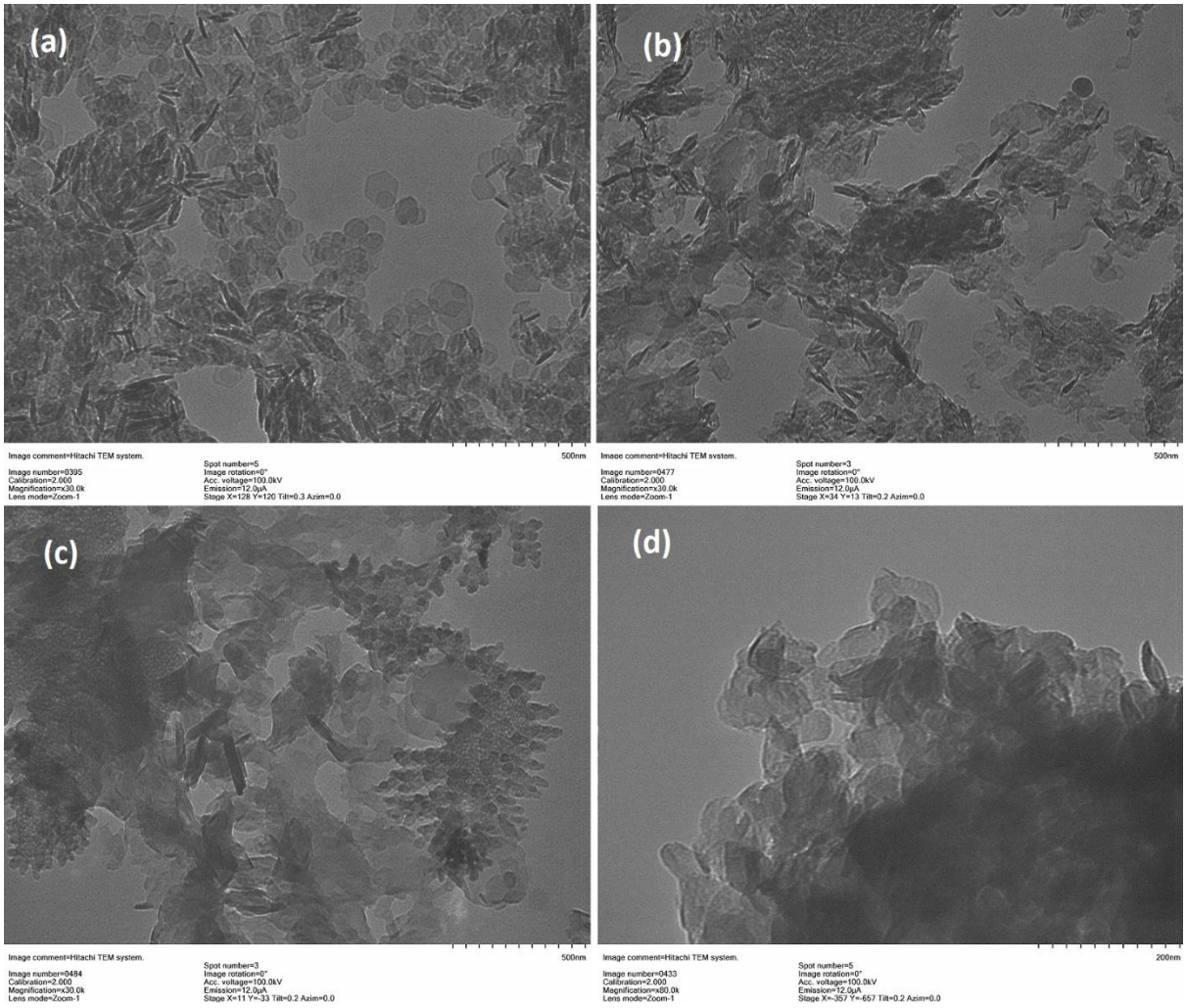

Figure 33. TEM pictures of typical cellulose-MH nanocomposite with different morphology types of intercalated nanosized $Mg(OH)_2$: (a) rod like and hexagonal nanostructures, (b,c) spherical crystals, (d) embedded MH particles with cellulose.

Figure 34 shows the SEM images of cellulose-MH sample with different magnification. As shown in Fig. 34 (a) magnesium hydroxide crystals are fully integrated into cellulose matrix for all the samples. From magnified micrographs Fig. 34 (b-d) intercalated $Mg(OH)_2$ can be clearly observed. According to SEM, the average size of MH nanostructures does not exceed 50 nm. Microscopy images indicate the successful synthesis of cellulose-MH nanocomposites and increase of the porosity. The results of the both TEM and SEM are well matched with the XRD results.

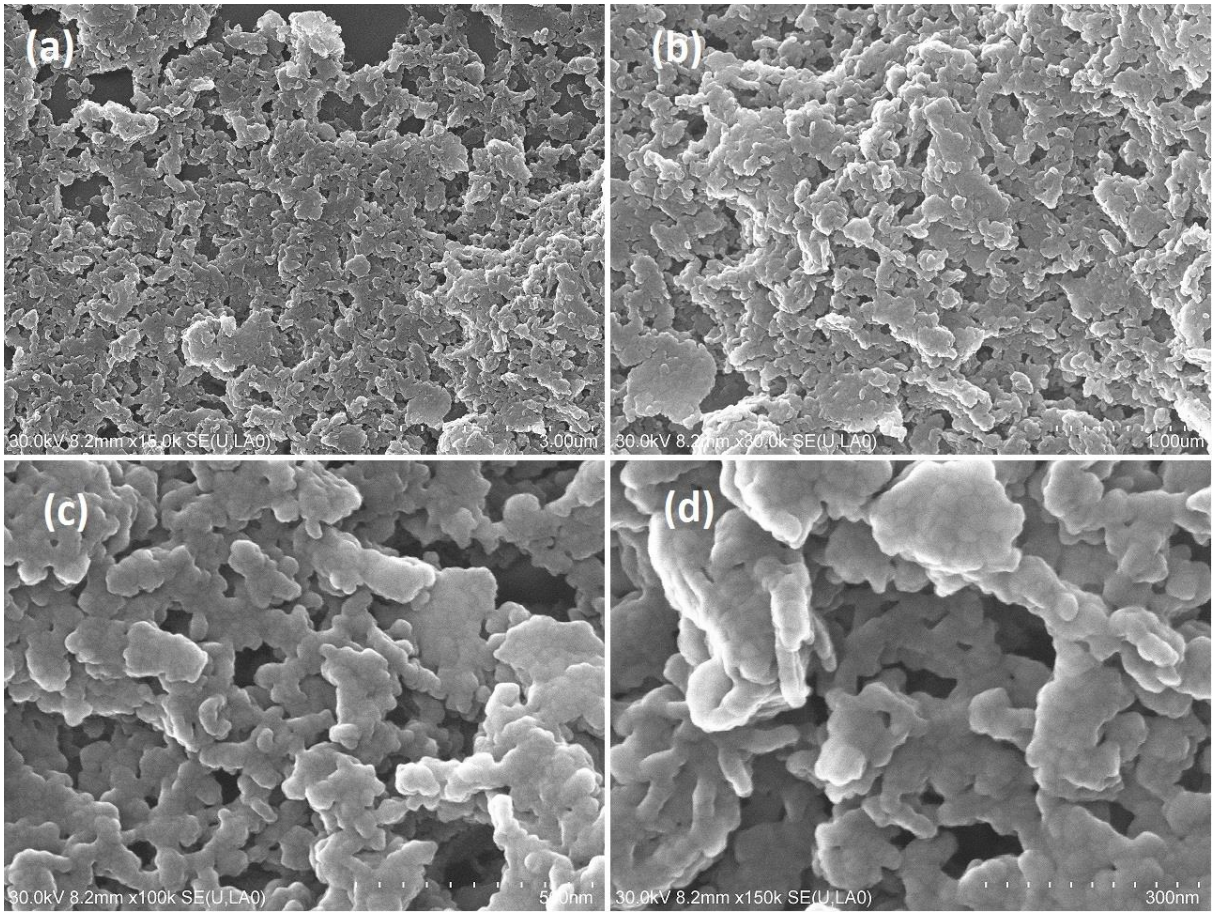

Figure 34. SEM pictures of CL-MH sample with various magnification: (a) 15k; (b) 30k; (c) 100k; (d) 150k.

5.4.5. EDS studies

Figure 35 shows EDS elemental spectrum and mapping of cellulose-MH sample prepared at 65 °C for 24 hours. According to the elemental analyses, one can observe the following elements: C, Mg, O, and Ag in the EDS spectrum (Fig. 35 (a)). The Ag peak is assigned to the sample preparation technique for the SEM analysis. Other elements are attributed to the cellulose-MH nanocomposite and prove the right composition. The strong observed peak of Mg element indicates the presence of magnesium in nanocomposite. Figure 35 (b-d) shows the EDS elemental mapping images of C, Mg and O. According to the magnesium EDS mapping (Fig. 35 (c)), Mg nanostructures are evenly distributed in the cellulose matrix that further confirms the proper composition of cellulose-MH nanocomposite. The EDS mappings of oxygen and carbon (Fig 35 (a), (d)) also prove the correct composition and even distribution of elements in the cellulose-MH sample.

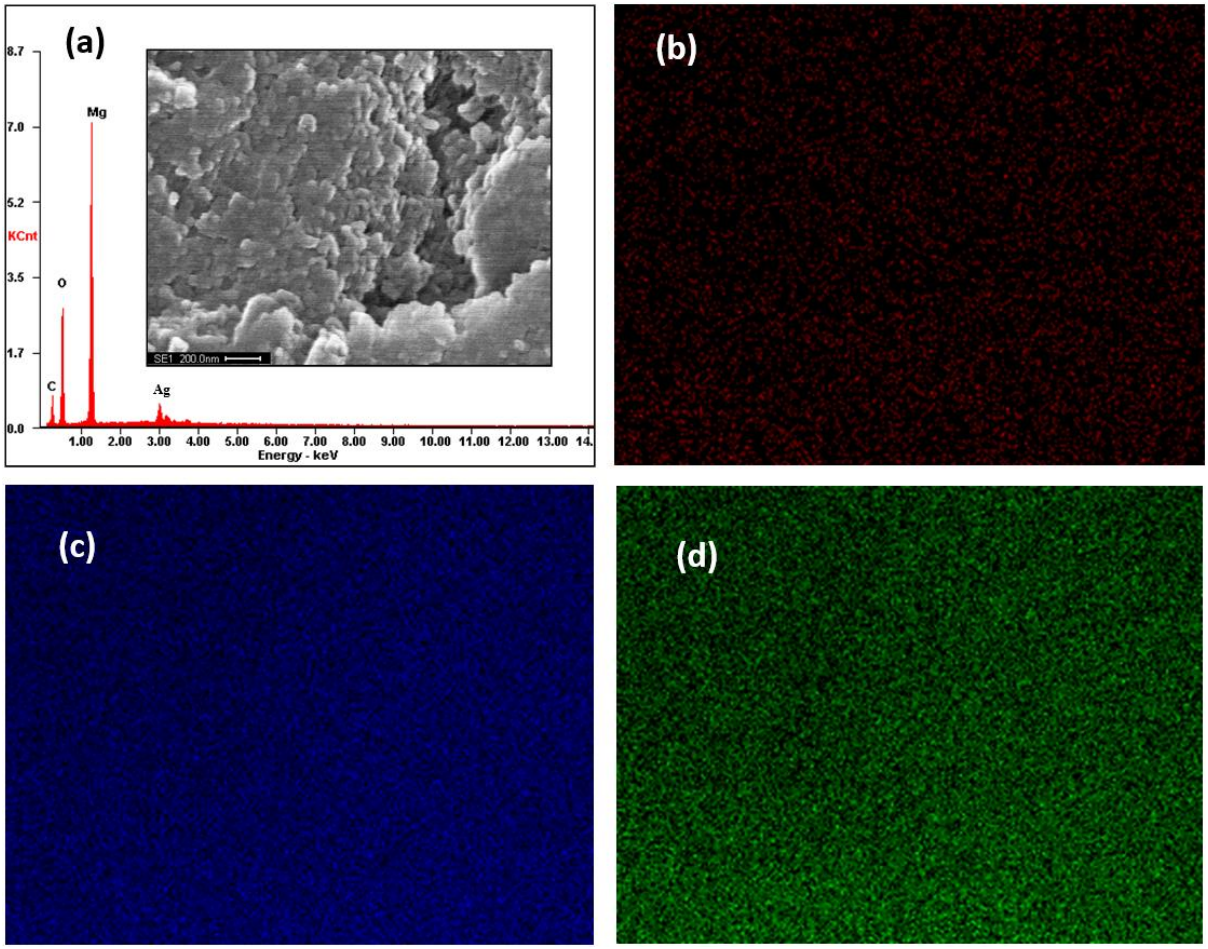

Figure 35. (a) EDS spectrum and (b-d) the EDS elemental mapping images of the cellulose-MH nanocomposite prepared at 65 °C for 24 h: (b) C; (c) Mg; (d) O.

6. Conclusions and the further research

As a summary, a new, simple, cost-efficient and environmentally friendly thermal-assisted technique for the synthesis of novel cellulose-based nanocomposites was reported. FTIR analysis confirmed the right chemical composition for each material and TEM showed the structure corresponding to nanocomposites. All the cellulose based materials with different reinforcements were tested as adsorbents and demonstrated a sufficient adsorption performance.

Based on the initial adsorption experiments and the careful evaluation of the advantages and disadvantages of the studied materials, cellulose-magnesium hydroxide nanocomposite was selected for the more detailed studies. The XRD, FTIR and EDS elemental analysis confirmed the structure of the cellulose-MH nanocomposites and the SEM and TEM micrographs showed even distribution of $Mg(OH)_2$ nanostructures in the cellulose matrix. The cellulose-based $Mg(OH)_2$ composite devoid of a typical nano-scaled magnesium hydroxide agglomeration of nano-crystals to large particles. Cellulose was strongly bonded with $Mg(OH)_2$ by hydrogen bonds, which provides a significant strength and durability for the nanocomposites. Furthermore, the obtained results demonstrated the applicability of "green" PEG/NaOH solvent in the preparation of cellulose based nanocomposites.

According to this research, studied nanocomposites have a great potential in different application fields such as water treatment, catalysis, medicine and so on. There are lot of never studied polymers and reinforcements with incredible properties, which can be applied for nanocomposites synthesis. Various preparation methods should be conducted and optimum process conditions investigated to find the most optimal technique, which makes possible the industrial applications of these materials. Nanocomposites are promising for the water purification. Therefore, novel materials should be tested with different pollutants such as organic and inorganic, other anions and cations. Deeper adsorption studies of nanocomposites such as kinetics, thermodynamics, pH and so on should also be investigated for further pilot tests and process design. In addition, deeper studies are needed for this topic.

References

Attia, M. F., Azib, T., Salmi, Z., Singh, A., Decorse, P., Battaglini, N., … Chehimi, M. M. (2013). One-step UV-induced modification of cellulose fabrics by polypyrrole/silver nanocomposite films. *Journal of Colloid and Interface Science*, *393*(1), 130–137. https://doi.org/10.1016/j.jcis.2012.11.008

Bish, D.L. (1980) Anion-exchange in takovite: applications to other hydroxide minerals (*). *Bulletin of The Mineral Research and Exploration, 103, 170-175.*

Buchanan, R. a., Caspers, H. H., & Murphy, J. (1963). Lattice Vibration Spectra of Mg(OH)_2 and Ca(OH)_2. *Applied Optics*, *2*(11), 1147. https://doi.org/10.1364/AO.2.001147

Cai, J., Liu, S., Feng, J., Kimura, S., Wada, M., Kuga, S., & Zhang, L. (2012). Cellulose-silica nanocomposite aerogels by in-situ formation of silica in cellulose gel. *Angewandte Chemie - International Edition*, *51*(9), 2076–2079. https://doi.org/10.1002/anie.201105730

Cai, J., & Zhang, L. (2005). Rapid dissolution of cellulose in LiOH/urea and NaOH/urea aqueous solutions. *Macromolecular Bioscience*, *5*(6), 539–548. https://doi.org/10.1002/mabi.200400222

Cavani, F., Trifiro, F., & Vaccari, A. (1991). Hydrotalcite-type anionic clays: Preparation, properties and applications. *Catalysis Today*, *11*(2), 173–301. https://doi.org/10.1016/0920-5861(91)80068-K

Cuculo, J. A., Smith, C. B., Sangwatanaroj, U., Stejskal, E. O., & Sankar, S. S. (1994). A study on the mechanism of dissolution of the cellulose/NH3/NH4SCN system. I. *Journal of Polymer Science Part A: Polymer Chemistry*, *32*(2), 229–239. https://doi.org/10.1002/pola.1994.080320203

Deng, Y. F., Zhang, Y., Cui, X., Shi, F., & Deng, Y. (2011). Nano-Gold Catalysis in Fine Chemical Synthesis Nano-Gold Catalysis in Fine Chemical Synthesis, (March 2015), 2467–2505. https://doi.org/10.1021/cr200260m

Ding, Y., Zhang, G., Wu, H., Hai, B., Wang, L., & Qian, Y. (2001). Nanoscale magnesium hydroxide and magnesium oxide powders: Control over size, shape, and structure via hydrothermal synthesis. *Chemistry of Materials*, *13*(2), 435–440. https://doi.org/10.1021/cm000607e

Du, L., Qu, B., Meng, Y., & Zhu, Q. (2006). Structural characterization and thermal and mechanical properties of poly(propylene carbonate)/MgAl-LDH exfoliation nanocomposite via solution intercalation. *Composites Science and Technology*, *66*(7–8), 913–918. https://doi.org/10.1016/j.compscitech.2005.08.012

Eichhorn, S. J., Dufresne, A., Aranguren, M., Marcovich, N. E., Capadona, J. R., Rowan, S. J., … Peijs, T. (2010). *Review: Current international research into cellulose nanofibres and nanocomposites*. *Journal of Materials Science* (Vol. 45). https://doi.org/10.1007/s10853-009-3874-0

Fu, L.-H., Yao, K., Shi, C.-M., Ma, M.-G., & Zhao, J.-J. (2014). Ultrasonic-assisted synthesis of cellulose/Cu (OH) 2/CuO hybrids and its thermal transformation to CuO and Cu/C. *Science of Advanced Materials*, *6*(6), 1117–1125. https://doi.org/10.1166/sam.2014.1875

Fu, L. H., Dong, Y. Y., Ma, M. G., Yue, W., Sun, S. L., & Sun, R. C. (2013). Why to synthesize vaterite polymorph of calcium carbonate on the cellulose matrix via sonochemistry process? *Ultrasonics Sonochemistry*, *20*(5), 1188–1193. https://doi.org/10.1016/j.ultsonch.2013.03.008

Fu, X., & Qutubuddin, S. (2000). Synthesis of polystyrene-clay nanocomposites. *Materials Letters*, *42*(1), 12–15. https://doi.org/10.1016/S0167-577X(99)00151-2

Grande, C. J., Torres, F. G., Gomez, C. M., & Carmen Bañó, M. (2009). Nanocomposites of bacterial cellulose/hydroxyapatite for biomedical applications. *Acta Biomaterialia*, *5*(5), 1605–1615. https://doi.org/10.1016/j.actbio.2009.01.022

Han, D., & Yan, L. (2010). Preparation of all-cellulose composite by selective dissolving of cellulose surface in PEG/NaOH aqueous solution. *Carbohydrate Polymers*, *79*(3), 614–619. https://doi.org/10.1016/j.carbpol.2009.09.008

Hattori, M., Koga, T., Shimaya, Y., & Saito, M. (1998). Aqueous Calcium Thiocyanate Solution as a Cellulose Solvent. Structure and Interactions with Cellulose. *Polym J*. https://doi.org/10.1295/polymj.30.43

Heinze, T., Dicke, R., Koschella, A., Kull, A. H., Klohr, E.-A., & Koch, W. (2000). Effective preparation of cellulose derivatives in a new simple cellulose solvent. *Macromolecular Chemistry and Physics*, *201*, 627–631. https://doi.org/10.1002/(sici)1521-3935(20000301)201:6<627::aid-macp627>3.0.co;2-y

Hokkanen, S., Repo, E., Westholm, L. J., Lou, S., Sainio, T., & Sillanpää, M. (2014). Adsorption of Ni2+, Cd2+, PO43- and NO3- from aqueous solutions by nanostructured microfibrillated cellulose modified with carbonated hydroxyapatite. *Chemical Engineering Journal*, *252*, 64–74. https://doi.org/10.1016/j.cej.2014.04.101

Hua, M., Zhang, S., Pan, B., Zhang, W., Lv, L., & Zhang, Q. (2012). Heavy metal removal from water/wastewater by nanosized metal oxides: A review. *Journal of Hazardous Materials*, *211–212*, 317–331. https://doi.org/10.1016/j.jhazmat.2011.10.016

Iftekhar, S., Srivastava, V., & Sillanpää, M. (2017). Synthesis and application of LDH intercalated cellulose nanocomposite for separation of rare earth elements (REEs). *Chemical Engineering Journal*, *309*, 130–139. https://doi.org/10.1016/j.cej.2016.10.028

Jahed, E., Khaledabad, M. A., Almasi, H., & Hasanzadeh, R. (2017). Physicochemical properties of Carum copticum Essential Oil Loaded Chitosan Films Containing Organic Nanoreinforcements. *Carbohydrate Polymers*, *164*, 325–338. https://doi.org/10.1016/j.carbpol.2017.02.022

Jang, S. H., Min, B. G., Jeong, Y. G., Lyoo, W. S., & Lee, S. C. (2008). Removal of lead ions in aqueous solution by hydroxyapatite/polyurethane composite foams. *Journal of Hazardous Materials*, *152*(3), 1285–1292. https://doi.org/10.1016/j.jhazmat.2007.08.003

Jeon, I. Y., & Baek, J. B. (2010). Nanocomposites derived from polymers and inorganic nanoparticles. *Materials*, *3*(6), 3654–3674. https://doi.org/10.3390/ma3063654

Jia, N., Li, S. M., Zhu, J. F., Ma, M. G., Xu, F., Wang, B., & Sun, R. C. (2010). Microwave-assisted synthesis and characterization of cellulose-carbonated hydroxyapatite nanocomposites in NaOH-urea aqueous solution. *Materials Letters*, *64*(20), 2223–2225. https://doi.org/10.1016/j.matlet.2010.07.029

Jia, N., Li, S., Ma, M., Sun, R., & Zhu, J. (2010). Hydrothermal Synthesis and

Characterization of Cellulose-Carbonated Hydroxyapatite Nanocomposites in NaOH – Urea Aqueous Solution, (Cmc), 210–214. https://doi.org/10.1166/sam.2010.1086

Kołodyńska, D., Gęca, M., Pylypchuk, I. V, & Hubicki, Z. (2016). Development of New Effective Sorbents Based on Nanomagnetite. *Nanoscale Research Letters*, *11*(1), 152. https://doi.org/10.1186/s11671-016-1371-3

Langford, J. I., & Wilson, A. J. C. (1978). Scherrer after sixty years: A survey and some new results in the determination of crystallite size. *Journal of Applied Crystallography*, *11*(2), 102–113. https://doi.org/10.1107/S0021889878012844

Lefatshe, K., Muiva, C. M., & Kebaabetswe, L. P. (2017). Extraction of Nanocellulose and In-Situ Casting of ZnO/Cellulose Nanocomposite with Enhanced Photocatalytic and Antibacterial Activity. *Carbohydrate Polymers*, *164*, 301–308. https://doi.org/10.1016/j.carbpol.2017.02.020

Li, S. M., Jia, N., Zhu, J. F., Ma, M. G., & Sun, R. C. (2010). Synthesis of cellulose-calcium silicate nanocomposites in ethanol/water mixed solvents and their characterization. *Carbohydrate Polymers*, *80*(1), 270–275. https://doi.org/10.1016/j.carbpol.2009.11.024

Liang, X., Zang, Y., Xu, Y., Tan, X., Hou, W., Wang, L., & Sun, Y. (2013). Sorption of metal cations on layered double hydroxides. *Colloids and Surfaces A: Physicochemical and Engineering Aspects*, *433*(31), 122–131. https://doi.org/10.1016/j.colsurfa.2013.05.006

Liu, S., Cai, P., Li, X., Chen, L., Li, L., & Li, B. (2016). Effect of film multi-scale structure on the water vapor permeability in hydroxypropyl starch (HPS)/Na-MMT nanocomposites. *Carbohydrate Polymers*, *154*, 186–193. https://doi.org/10.1016/j.carbpol.2016.08.006

Liu, S., Zhang, L., Zhou, J., & Wu, R. (2008). Structure and properties of cellulose/Fe2O3 nanocomposite fibers spun via an effective pathway. *Journal of Physical Chemistry C*, *112*(12), 4538–4544. https://doi.org/10.1021/jp711431h

Ma, M. G., Deng, F., & Yao, K. (2014). Manganese-containing cellulose nanocomposites: The restrain effect of cellulose treated with NaOH/urea aqueous solutions. *Carbohydrate Polymers*, *111*, 230–235. https://doi.org/10.1016/j.carbpol.2014.04.080

Ma, M. G., Zhu, J. F., Jia, N., Li, S. M., Sun, R. C., Cao, S. W., & Chen, F. (2010). Rapid microwave-assisted synthesis and characterization of cellulose-hydroxyapatite nanocomposites in N,N-dimethylacetamide solvent. *Carbohydrate Research*, *345*(8), 1046–1050. https://doi.org/10.1016/j.carres.2010.03.004

Marques, P. A. A. P., Trindade, T., & Neto, C. P. (2006). Titanium dioxide/cellulose nanocomposites prepared by a controlled hydrolysis method. *Composites Science and Technology*, *66*(7–8), 1038–1044. https://doi.org/10.1016/j.compscitech.2005.07.029

Mccormick, C. L., & Hutchinson, B. H. (1985). Solution Studies of Cellulose in Lithium Chloride and N,N-Dimethylacetamide. *Macromolecules*, *18*(1529), 2394–2401. https://doi.org/10.1021/ma00154a010

Nata, I. F., Sureshkumar, M., & Lee, C.-K. (2011). One-pot preparation of amine-rich magnetite/bacterial cellulose nanocomposite and its application for arsenate removal. *RSC Advances*, *1*(4), 625–631. https://doi.org/10.1039/c1ra00153a

Okamoto, M., Morita, S., Kim, Y. H., Kotaka, T., & Tateyama, H. (2000). Synthesis and

structure of smectic clay/poly(methyl methacrylate) and clay/polystyrene nanocomposites via in situ intercalative polymerization. *Polymer*, *41*(10), 3887–3890. https://doi.org/10.1016/S0032-3861(99)00655-2

Papko, A. P. (2013) Phisico-khemicheskie metodi issledovaniya neorganicheskikh veshestv i materialov (In Russian). Praktikum (book). *BGTU, Minsk, Belarussia, 95 pages.*

Park, M., Choi, C. L., Seo, Y. J., Yeo, S. K., Choi, J., Komarneni, S., & Lee, J. H. (2007). Reactions of Cu2+ and Pb2+ with Mg/Al layered double hydroxide. *Applied Clay Science*, *37*(1–2), 143–148. https://doi.org/10.1016/j.clay.2006.12.006

Siqueira, G., Mathew, A. P., & Oksman, K. (2011). Processing of cellulose nanowhiskers/cellulose acetate butyrate nanocomposites using sol-gel process to facilitate dispersion. *Composites Science and Technology*, *71*(16), 1886–1892. https://doi.org/10.1016/j.compscitech.2011.09.002

Sureshkumar, M., Siswanto, D. Y., & Lee, C.-K. (2010). Magnetic antimicrobial nanocomposite based on bacterial cellulose and silver nanoparticles. *Journal of Materials Chemistry*, *20*(33), 6948. https://doi.org/10.1039/c0jm00565g

Svagan, A. J., Jensen, P., Dvinskikh, S. V., Furó, I., & Berglund, L. A. (2010). Towards tailored hierarchical structures in cellulose nanocomposite biofoams prepared by freezing/freeze-drying. *Journal of Materials Chemistry*, *20*, 6646–6654. https://doi.org/10.1039/c0jm00779j

Wang, P. ., Ye, Y. ., Liang, D. . b, Sun, H. . b, Liu, J. ., Tian, Z. ., & Liang, C. . b. (2016). Layered mesoporous Mg(OH)2/GO nanosheet composite for efficient removal of water contaminants. *RSC Advances*, *6*(32), 26977–26983. https://doi.org/10.1039/c6ra02914k

Yan, L., & Gao, Z. (2008). Dissolving of cellulose in PEG/NaOH aqueous solution. *Cellulose*, *15*(6), 789–796. https://doi.org/10.1007/s10570-008-9233-5

Yano, K., Usuki, A., & Okada, A. (1997). Synthesis and Properties of Polyimide-Clay Hybrid Films. *J Polym Sci A: Polym Chem*, *35*(January 1997), 2289–2294. https://doi.org/10.1002/(SICI)1099-0518(199708)35:11<2289::AID-POLA20>3.0.CO;2-9

Zhang, T., Wang, W., Zhang, D., Zhang, X., Yurong, M., Zhou, Y., & Qi, L. (2010). Biotemplated synthesis of cold nanoparticle-bacteria cellulose nanofiber nanocomposites and their application in biosensing. *Advanced Functional Materials*, *20*(7), 1152–1160. https://doi.org/10.1002/adfm.200902104

Zheng, J., & Zhou, W. (2014). Solution-phase synthesis of magnesium hydroxide nanotubes. *Materials Letters*, *127*, 17–19. https://doi.org/10.1016/j.matlet.2014.04.076